



Catalyst-assisted chemical looping auto-thermal dry reforming: Spatial structuring effects on process efficiency

Jiawei Hu^a, Vladimir V. Galvita^{a,*}, Hilde Poelman^a, Christophe Detavernier^b, Guy B. Marin^a

^a Laboratory for Chemical Technology, Ghent University, Technologiepark 914, B-9052 Ghent, Belgium

^b Department of Solid State Sciences, Ghent University, Krijgslaan 281, S1, B-9000 Ghent, Belgium



ARTICLE INFO

Keywords:

Auto-thermal dry reforming
Chemical looping
Process efficiency
Spatial structuring
Ni-Fe bifunctional catalyst
Core-shell structure

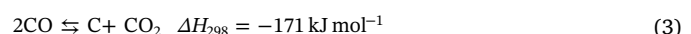
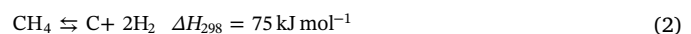
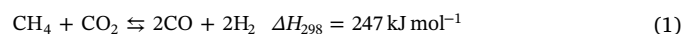
ABSTRACT

Catalyst-assisted chemical looping auto-thermal dry reforming (CCAR) is an environment-friendly energy conversion process, performed over a reactor bed with double function, composed of a catalyst and an oxygen storage material (OSM). It converts CH_4 and CO_2 into industrial syngas, while simultaneously utilizing CO_2 from the atmosphere. Two reactor bed configurations were tested, based on the concept of double- and single-zone distribution of catalyst and OSM. Combinations of core-shell structured materials were applied, such as Ni/ ZrO_2 @ ZrO_2 catalyst, Fe_2O_3 / ZrO_2 @ ZrO_2 OSM and Fe/Zr@Zr-Ni@Zr bifunctional catalyst, to assess the spatial structuring at both reactor bed and pellet scale. Samples from different reactor beds were characterized before and after use by ex- or in-situ XRD, N_2 adsorption, XPS and STEM-EDX. 25 redox cycles of CCAR were performed to investigate the effect of spatial structuring on the activity and stability. The Fe/Zr@Zr-Ni@Zr bifunctional catalyst possesses higher activity and stability for catalytic CH_4 conversion in the reduction half-cycle than the Ni/ ZrO_2 @ ZrO_2 catalyst due to its small Ni particle size ($< 3 \text{ nm}$), high carbon resistance and thermal stability of the eccentric core-shell structure. A double-zone bed with Ni/ ZrO_2 @ ZrO_2 catalyst and Fe_2O_3 / ZrO_2 @ ZrO_2 OSM has a similar activity as a single-zone bed for producing syngas in the reduction half-cycle, but it presents a higher CO yield in the re-oxidation half-cycle. This is due to the full use of the oxygen storage capacity of the OSM achieved by complete reduction of Fe_3O_4 and the avoiding of Ni-Fe alloy formation during the reduction half-cycle. A double-zone bed with bifunctional catalyst and OSM combines both advantages. It provides the highest activity and stability for auto-thermal dry reforming and the highest oxygen storage capacity for CO_2 utilization, offering a promising reactor technology for the CCAR process.

1. Introduction

Considering the depletion of fossil fuels and the growing concern about environmental impact during energy conversion processes, there is need to investigate more efficient ways to utilize available energy resources, such as natural gas, with low environmental impact [1,2]. Dry reforming of methane is a high value-added energy conversion process as it not only utilizes two abundantly available greenhouse gases (CO_2 and CH_4), thereby supporting efforts of environmental protection, but also produces a crucial chemical intermediate resource, industrial syngas (a mixture of H_2 and CO), which is suitable for further use in e.g. hydroformylation and carbonylation processes and the synthesis of liquid fuels [3–9]. However, methane dry reforming is a strongly endothermic process (Eq. (1)), from thermodynamic considerations, requiring high temperature to obtain high CH_4 and CO_2 conversion [8,10], leading to large energy consumption. Such high temperatures also result in catalyst deactivation due to active metal

sintering and coke formation through CH_4 decomposition (Eq. (2)) or CO disproportionation (Eq. (3)) [11–13].



This drawback can be overcome by co-feeding oxygen, which renders the process auto-thermal, in close analogy to industrial auto-thermal CH_4 reforming [14–16]. Hence, a process combining dry and auto-thermal reforming of methane, i.e. auto-thermal dry reforming, was proposed, where a small amount of O_2 was co-fed with CH_4 and CO_2 to partially convert CH_4 in an exothermic reaction (partial oxidation (Eq. (4)) or combustion (Eq. (5))) [8,15,17–20], generating heat in-situ and thereby compensating the strong endothermicity of the dry reforming reaction for a net $\Delta H = 0 \text{ kJ mol}^{-1}$. Moreover, in the

* Corresponding author.

E-mail address: Vladimir.Galvita@UGent.be (V.V. Galvita).

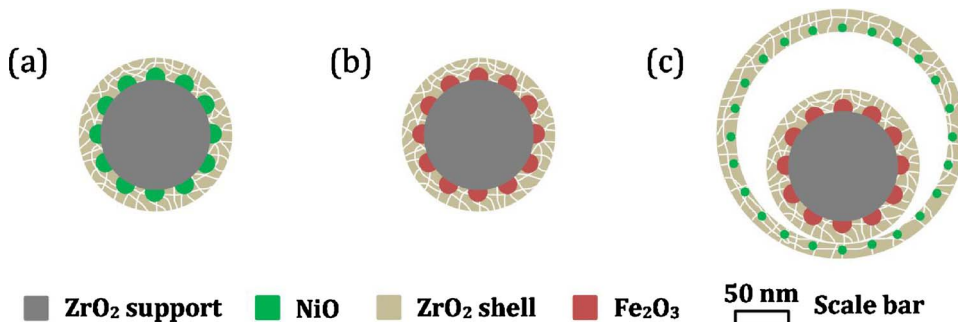
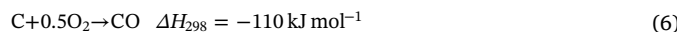
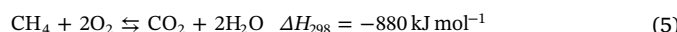
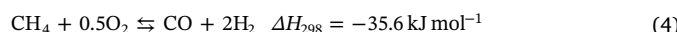
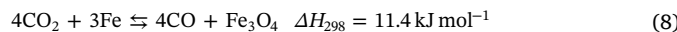
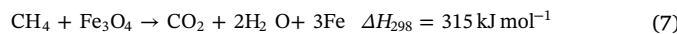


Fig. 1. Schematic representation of spatial structuring at pellet scale: catalyst and OSM as core-shell structured materials: (a) Ni-based catalyst, (b) Fe-based OSM and (c) Ni-Fe bifunctional catalyst.

presence of O_2 , the carbon oxidation reaction (Eq. (6)) can occur to help eliminate coke formation.



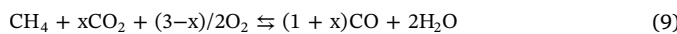
Another approach is performing methane dry reforming in a chemical looping process, so called chemical looping dry reforming [14,21–23]. Such process is based on periodic reduction/re-oxidation cycling of an oxygen storage material (OSM), which is divided into two, spatially or temporally separated half-cycles [2,24]: CH_4 reduces the OSM (e.g. Fe_3O_4) and produces CO_2 and H_2O during the reduction half-cycle (Eq. (7)), after which the material is regenerated by CO_2 , simultaneously producing CO , in the re-oxidation half-cycle (Eq. (8)).



Application of chemical looping dry reforming brings several advantages: First, since the OSM is regenerated in each cycle, deposited carbon can be removed by reacting with CO_2 (reverse Eq. (3)). Second, as CO_2 is used as an oxidizing agent for material regeneration in the re-oxidation half-cycle, this process can utilize more CO_2 (three molecules of CO_2 per molecule of CH_4) than conventional dry reforming of methane.

A key issue in chemical looping dry reforming is the selection of an appropriate OSM. The reactivity and thermal stability of the OSM, as well as its cost are critical selection criteria. While a number of metal oxides, such as Fe_3O_4 [24–27], NiO [28–30], CoO [21], Mn_3O_4 [31,32] and CuO [33,34], hold CO_2 reduction capacity, it was found that iron oxide presents the highest oxygen storage capacity from CO_2 (0.7 mol CO_2 /mol Fe) over a broad range of operating temperatures (600–1800 °C) [25]. Thus, chemical looping dry reforming over iron oxide as OSM has been one of the target technologies for CO_2 utilization.

Given the above background, it is clear that chemical looping dry reforming is optimized for maximum utilization of CO_2 feedstock during CH_4 reforming, while eliminating the deposited carbon in the re-oxidation half-cycle. However, the high heat requirement of the reaction (Eq. (7)) in the reduction half-cycle remains an issue. In comparison, auto-thermal dry reforming can achieve in-situ carbon removal and heat compensation at the same time, but the conversion of CO_2 is suppressed owing to the presence of O_2 (Eq. (5)). Hence, an intensified process, termed chemical looping auto-thermal dry reforming (Eq. (9)), was designed to combine the complementary advantages of both technologies for utilizing CH_4 and CO_2 in an efficient and low energy consuming way [16,35].



Thermodynamic analysis shows that the whole process can operate in thermoneutral condition, i.e. $\Delta H = 0 \text{ kJ mol}^{-1}$, at 600 and 750 °C, with a value of $x = 2.4$ and 2, respectively [35].

A mixture of CH_4 , CO_2 and a small amount of O_2 is converted to syngas and simultaneously the iron oxide OSM is reduced during the reduction half-cycle. In the re-oxidation half-cycle, extra CO_2 is fed to re-oxidize the material and produce CO . However, from a kinetic point of view, the reduction rate of iron oxide is slow when using CH_4 as reducing gas, and even becomes slower in the presence of CO_2 and O_2 , because both act as oxidizing agent, hence significantly decreasing the rate of iron oxide reduction, and accordingly decreasing the achieved degree of the reduction for a given reduction time. The latter plays a crucial role in the conversion of CO_2 to CO during the re-oxidation half-cycle. This limitation can be overcome by performing the process over a bifunctional reactor bed, composed of either a physical mixture of a Ni-based catalyst and a Fe-based OSM, or a bifunctional Ni-Fe material [2,36,37]. Therefore, a new process, catalyst-assisted chemical looping auto-thermal dry reforming (CCAR), has been proposed [35]. During the reduction half-cycle, CH_4 , CO_2 and O_2 are converted over the Ni catalyst into H_2 and CO , which both reduce the iron oxide OSM. The reduction of iron oxide by H_2 and CO is substantially faster and deeper than by CH_4 [2,38], which stresses the importance of the Ni catalyzed CH_4 reforming process.

A chemical looping process can be implemented in different reactor concepts: a rotating reactor, a fluidized bed or a fixed bed reactor [39,40]. Here, we study the CCAR process in the fixed bed reactor. The key focus of the present work goes to the optimal spatial structuring of the Ni catalyst and iron oxide OSM at both reactor bed and pellet scale. The former affects the efficiency of the CH_4 conversion and CO_2 utilization, in terms of CO yield. The latter ensures the stability of the materials and hence of the entire process. In previous work, a Ni-Fe/ $MgAl_2O_4$ bifunctional material was used in the CCAR process, which suffered from severe deactivation after 25 cycles at 750 °C due to particle sintering [35]. In the present study, a combination of impregnation and nanocoating is used to synthesize the Ni-based catalyst (Fig. 1a) and Fe-based OSM (Fig. 1b), both with a core-shell structure, consisting of an active metal core and an inert shell. Such structures have been confirmed to show high reactivity and stability in methane reforming and chemical looping processes [22,24,41–44].

These catalyst and OSM materials are used to establish two reactor bed configurations, based on the concept of double- or single-zone bed, to investigate the effect of the spatial distribution of catalyst and OSM in the reactor bed on the process efficiency, in terms of CH_4 and CO_2 conversion to CO . As illustrated in Fig. 2, the difference in reactor configuration mainly depends on the working mode of the reduction half-cycle. For the double-zone bed (Fig. 2a), the mixture feed CH_4 , CO_2 and O_2 is converted in the first zone over Ni to CO and H_2 , which then both flow into the second zone to reduce the iron oxide to metallic iron. For the single-zone bed (Fig. 2b), the generated CO and H_2 are immediately consumed by the contiguous iron oxide. Based on Le Chatelier's principle, this in-situ H_2 and CO consumption promotes a

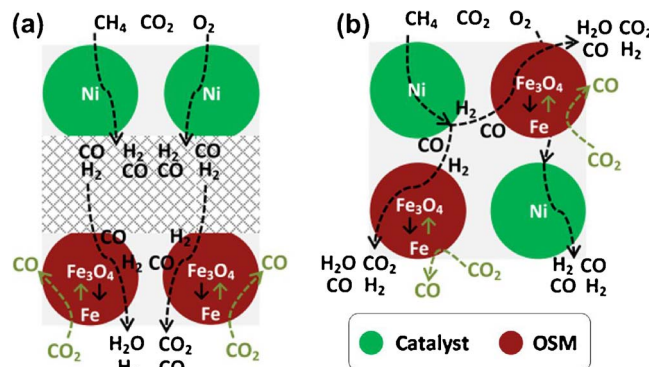


Fig. 2. Schematic representation of the spatial structuring of catalyst and OSM at reactor bed scale for catalyst-assisted chemical looping auto-thermal dry reforming: (a) double-zone and (b) single-zone catalyst and OSM reactor bed. The black and green arrows represent the reaction route in the reduction half-cycle (auto-thermal dry reforming and Fe_3O_4 reduction) and the re-oxidation half-cycle (re-oxidation of Fe to Fe_3O_4 by CO_2 and CO production), respectively. (For interpretation of the references to colour in this figure legend, the reader is referred to the web version of this article.)

positive equilibrium shift of the reforming reaction (Eq. (1)), thereby enhancing the conversion of CH_4 and CO_2 . Furthermore, in order to exploit a similar equilibrium shift to enhance the catalyst activity during CCAR, a core-shell structured Ni-Fe bifunctional nanomaterial (Fig. 1c), containing a Fe-based core encapsulated by a separate Ni-based outer shell, is designed as improved catalyst. Several advantages steer the selection of such particular structure: (1) the Ni-based shell and the Fe-based core respectively act as reforming catalyst and OSM, expected to achieve catalytic reforming and consumption of H_2 and CO in a single nanoscale unit; (2) the hollow sphere, enclosing the core, not only prevents the aggregation of Fe-based OSM particles [45], but also provides sufficient space to ensure contact between reactant gases and the core; (3) the large specific surface area of the hollow sphere promotes the fine dispersion of Ni particles and the adequate deposition of the outer ZrO_2 protective layer, both of which contribute to retain a high catalytic activity [46]. Structural characterization of the materials as well as experimental performance data from the CCAR process in different reactor beds are reported.

2. Experimental procedure

2.1. Materials preparation

2.1.1. Support

A ZrO_2 support was prepared by precipitation through addition of excess ammonium hydroxide. Typically, 18.76 g of $\text{ZrO}(\text{NO}_3)_2 \cdot 6\text{H}_2\text{O}$ (Sigma-Aldrich, 99%) was dissolved in de-ionized water (300 mL) under stirring for 20 min. Afterwards, 10 mL of ammonia hydroxide solution (ACS reagent, 28.0–30.0% NH_3 basis) was added and the mixture was kept for 10 min under vigorous stirring. The formed precipitate was filtered, washed with de-ionized water, dried at 120 °C for 4 h and finally calcined in air at 900 °C (with a heating ramp of 5 °C min^{-1}) for 2 h to form a stable crystalline phase.

2.1.2. Core materials

Both 5 wt% NiO/ZrO_2 and 10 wt% $\text{Fe}_2\text{O}_3/\text{ZrO}_2$ core materials were prepared by incipient wetness impregnation on the as-prepared ZrO_2 support, using an aqueous solution containing the required amount of corresponding nitrates, $\text{Ni}(\text{NO}_3)_2 \cdot 6\text{H}_2\text{O}$ and $\text{Fe}(\text{NO}_3)_3 \cdot 9\text{H}_2\text{O}$ (Sigma-Aldrich, 99.99 +%). The impregnated samples were kept overnight at room temperature, then dried at 120 °C for 4 h and finally calcined in air at 400 °C (with a heating ramp of 1 °C min^{-1}) for 1 h.

2.1.3. Core-shell structured Ni-based catalyst and Fe-based OSM

The core materials NiO/ZrO_2 and $\text{Fe}_2\text{O}_3/\text{ZrO}_2$ were both coated with a ZrO_2 shell, yielding the core-shell $\text{Ni}/\text{ZrO}_2@/\text{ZrO}_2$ catalyst and core-shell $\text{Fe}_2\text{O}_3/\text{ZrO}_2@/\text{ZrO}_2$ OSM, respectively labeled as $\text{Ni}/\text{Zr}@\text{Zr}$ and $\text{Fe}/\text{Zr}@\text{Zr}$ (see the red lined region in Fig. 3). In brief, the powder of the core material (1 g) was dispersed in absolute ethanol (150 mL) in a single neck flask. Then, the flask was sealed with a cork and heated to 30 °C under vigorous stirring. Afterward, 1 mL of P-123 (Sigma-Aldrich, a nonionic amphiphilic surfactant, average molecular weight ~5800) aqueous solution (4 wt% in water) was added. After 1 h, 3.64 mL of zirconium propoxide solution (Sigma-Aldrich, 70 wt% in 1-propanol) was injected into the flask using a syringe, and the coating process was allowed to proceed for 20 h at 30 °C. The solid products were collected by filtration, washed with ethanol 3 times and subsequently calcined in air at 700 °C (with a heating ramp of 1 °C min^{-1}) for 4 h. A more

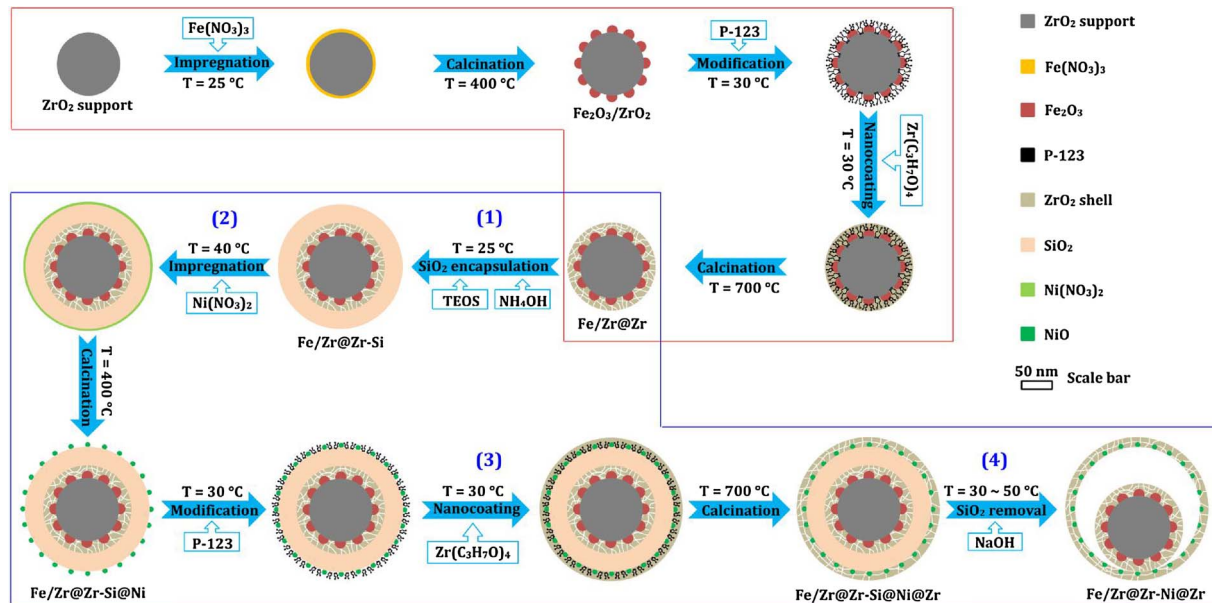


Fig. 3. Schematics of the synthesis of the proposed core-shell materials. The steps shown in the red lined region form the synthesis pathway of the $\text{Fe}/\text{Zr}@\text{Zr}$ core, and the following steps shown in the blue lined region constitute the synthesis procedure of the $\text{Fe}/\text{Zr}@\text{Zr-Ni}@\text{Zr}$ bifunctional catalyst, including four extra steps: (1)–(4). (For interpretation of the references to colour in this figure legend, the reader is referred to the web version of this article.)

detailed report on the synthesis method can be found in previous work [24].

2.1.4. Core-shell structured Ni-Fe bifunctional catalyst

The property of bifunction refers to the combined capability of catalytic methane conversion and oxygen storage. Based upon this concept, a core-shell bifunctional nanomaterial was designed, possessing a Fe/Zr@Zr OSM core and a ZrO₂-coated Ni shell, named as Fe/Zr@Zr-Ni@Zr (as seen in Fig. 3). To obtain such structure, a SiO₂ template-assisted method [47] is typically introduced in the synthesis pathway: the Fe/Zr@Zr core is first encapsulated in a dense SiO₂ layer using a slightly modified Stöber process [48], before impregnation with a Ni²⁺ aqueous solution. Finally, the SiO₂ is selectively removed from the product by dissolution with a solvent to expose the core, ensuring that it can contact with reactant gases. This results in an eccentric core-shell structure as the core is now no longer supported within the hollow shell.

The synthesis procedure includes four steps: First, the prepared Fe/Zr@Zr OSM (1 g) was dispersed in a mixture solution of de-ionized water (25 mL) and 2-propanol (100 mL, Sigma-Aldrich, 99.5%) in a single neck flask. To this solution, 4 mL of ammonia hydroxide solution was added under vigorous stirring at 25 °C. After 1 h, 10 mL of tetraethyl orthosilicate (TEOS) in 75 mL of 2-propanol was added over 6 h under stirring (which involved the addition of 21.25 mL every 2 h, i.e. for 4 times), and then stirring was continued for 20 h. The resulting precipitate was filtered, washed with ethanol 3 times and dried at 80 °C for 4 h, yielding approximately 4 g of SiO₂-coated material, labeled as Fe/Zr@Zr-Si.

In the second step, the Fe/Zr@Zr-Si particles (2 g) were impregnated with a Ni²⁺ aqueous solution, containing 0.0584 g of Ni (NO₃)₂·6H₂O, kept overnight at 40 °C and calcined at 400 °C (with a heating ramp of 0.5 °C min⁻¹) for 1 h. The impregnated sample was named as Fe/Zr@Zr-Si@Ni.

Third, the Fe/Zr@Zr-Si@Ni (0.9 g) was coated with a ZrO₂ nanoshell in a similar manner as in Section 2.1.3. The only difference is that the zirconium propoxide solution (3.64 mL) was injected into the flask over 6 h in 4 times (injection of 0.91 mL every 2 h). The resulting material was named Fe/Zr@Zr-Si@Ni@Zr.

In the final step, the removal of SiO₂ from the composite Fe/Zr@Zr-Si@Ni@Zr was achieved through a treatment with sodium hydroxide solution (1 mol L⁻¹) [49]. First, all samples were kept in NaOH solution (50 mL) for 20 h at 30 °C. Afterwards, the solution was replaced with a fresh one and the extraction was continued for another 20 h at 50 °C. Finally, the particles Fe/Zr@Zr-Ni@Zr were filtered, washed with de-ionized water (3 times) and ethanol (3 times) and dried at 120 °C for 24 h.

2.2. Ex-situ characterization

The actual chemical compositions of as-prepared materials were determined by means of inductively coupled plasma atomic emission spectroscopy (ICP-AES, ICAP 6500, Thermo Scientific). The samples were mineralized by peroxide fusion. The Brunauer-Emmett-Teller (BET) surface area of the samples was determined by N₂ adsorption at -196 °C (five point BET method using Gemini Micromeritics). Prior to analysis, the samples were outgassed at 200 °C for 2 h to eliminate volatile adsorbates from the surface. The crystallographic phases of the fresh and spent samples were determined by ex-situ XRD measurements using a Siemens Diffractometer Kristalloflex D5000, with Cu K α radiation. The powder XRD pattern was collected in a 2 θ range from 10° to 80° with a step of 0.02° and 30 s counting time per angle. By fitting a Gaussian function to a diffraction peak, the crystallite size can be determined from the peak width via the Scherrer equation [50].

Morphological, structural and local chemical analyses were carried out using transmission electron microscopy (TEM)-based methods: conventional TEM, scanning transmission bright field (STEM BF) and

energy dispersive X-ray analysis (EDX). These techniques were implemented using a JEOL JEM-2200FS Cs-corrected microscope operated at 200 kV, equipped with a Schottky-type field emission gun (FEG) and EDX JEOL JED-2300D. Specimens were prepared by immersion of a lacey carbon film on a copper support grid into the material powder followed by blowing off the excess powder. Particles sticking to the carbon film were investigated. A beryllium specimen retainer was used to eliminate secondary X-ray fluorescence in EDX spectra originating from the specimen holder.

XPS measurements were recorded with a S-Probe XPS spectrometer (VG, Surface Science Instruments), equipped with a monochromatized Al K α source. The base pressure of the analysis chamber was below 2×10^{-7} Pa. Spectra were recorded with 200 W source power. The analyzer axis made an angle of 45° with the specimen surface. Wide scan spectra were measured with a pass energy of 157 eV and a 0.22 eV step, while core levels were recorded with a step of 0.10 eV and a pass energy of 107.8 eV.

2.3. In-situ time-resolved XRD

Time-resolved crystallographic analyses of the tested materials were determined by means of in-situ X-ray diffraction (XRD) measurements in θ -2 θ mode using a Bruker-AXS D8 Discover apparatus with Cu K α radiation of wavelength 0.154 nm and a linear detector covering a range of 20° in 2 θ with an angular resolution of approximately 0.1°. The pattern collection time was typically 10 s. These in-situ experiments were carried out in a home-built reactor chamber with a Kapton foil window for X-ray transmission. Temperature was measured using a K-type thermocouple and corrected afterwards using a calibration curve. Approximately 20 mg of powdered sample was evenly spread on a single-crystal Si wafer. Interaction of these materials with the Si wafer was never observed. Before each experiment, the reactor chamber was evacuated to a base pressure of 4 Pa using a rotation pump. Gases were supplied to the reactor chamber from a rig with calibrated mass-flow meters.

The evolution of crystallographic changes of the materials was monitored during TPR, TPO and isothermal redox cycling. TPR was performed under flow conditions of 5% H₂/He (60 mL min⁻¹) up to a temperature of 800 °C at a heating rate of 20 °C min⁻¹. This was followed by TPO with 100% CO₂ at the same flow rate and heating up to 800 °C. Isothermal redox cycling was carried out at a temperature of 750 °C with alternating H₂ reduction and CO₂ re-oxidation sequences at a constant flow rate of 60 mL min⁻¹, before which the samples were heated to the targeted temperature at a rate of 60 °C min⁻¹ in He (60 mL min⁻¹). Each cycle (8 min in total) consisted of 2 min H₂ reduction, 2 min CO₂ re-oxidation and 2 min intermediate He purging.

2.4. Reactor setup and procedures

Activity measurements were performed at atmospheric pressure in a quartz tube microreactor (i.d. 10 mm), which was housed inside an electric furnace. Typically, 80 mg of sample, diluted with α -Al₂O₃ in a 1:20 ratio, was packed between quartz wool plugs. The temperature of the catalyst bed was measured with K-type thermocouples touching the outside and inside of the reactor at the position of the catalyst bed. The inlet gas flow rates were maintained by means of calibrated Bronkhorst mass flow controllers. The outlet gas stream was monitored online using an OmniStar Pfeiffer mass spectrometer (MS). The instrument was calibrated beforehand for different mixtures of reactants and products. H₂ was followed at 2, He at 4, CH₄ at 16, H₂O at 18, CO at 28, O₂ at 32, Ar at 40 and CO₂ at 44 AMU. Concentrations were determined taking into account the fragmentation patterns of the compounds, and a correction was applied to remove contributions from unavoidable interference with fragmentation peaks of other gases. The response of the mass spectrometer detector was regularly verified with calibration gases. The carbon balance was closed with a maximum deviation of

10%.

The activity is represented by the space-time yield (STY, $\text{mol s}^{-1} \text{kg}_M^{-1}$), calculated from the difference between the inlet and outlet molar flow rates, as measured relative to the internal standard Ar:

$$\text{STY}_i = \frac{|F_{0,i} - F_i|}{W_M} \quad (10)$$

where $F_{0,i}$ (mol s^{-1}) and F_i (mol s^{-1}) are the inlet and outlet molar flow rates of component i, and W_M (kg_M) is the mass of material in the reactor, i.e. Ni for the dry reforming process, Fe_2O_3 for the CO production during re-oxidation.

The activity and stability of the Ni/Zr@Zr catalyst and Fe/Zr@Zr-Ni@Zr bifunctional catalyst in methane dry reforming, i.e. corresponding to the reduction half-cycle of the CCAR process, are evaluated through a deactivation/regeneration experiment, combining methane reforming, material oxidation with O_2 for carbon removal and finally H_2 reduction for Ni activation. Three sequences of deactivation/regeneration were performed. First, the sample was reduced in a 180 mL min^{-1} flow of 10% H_2/Ar from room temperature to 750°C at a rate of $10^\circ\text{C min}^{-1}$ to reach the active state. After a 5 min purging step in Ar, a mixture of $\text{CH}_4:\text{CO}_2:\text{Ar}$ (molar ratio of 1:0.8:0.4, Ar is an internal standard) at a total flow rate of 150 mL min^{-1} was fed into the reactor and reaction took place at 750°C for 4 h. This feed was chosen to be CH_4 -rich ($\text{CH}_4:\text{CO}_2 = 1:0.8$), considering that CH_4 decomposition is the main source of carbon formation, and an important contributor to the deactivation of Ni-based catalysts during methane reforming [51] at this temperature [13]. Then, the deposited carbon was oxidized by 10% O_2/He (260 mL min^{-1}) for 10 min, while detecting the produced CO_2 in the outlet. Subsequently, the sample was regenerated in 10% H_2/Ar (180 mL min^{-1}) for 10 min before starting the next dry reforming sequence. The duration of the dry reforming reaction was reduced to 1 h in the second and third sequence. The CH_4 consumption rate (representative for activity) was calculated every 20 min of time on stream (TOS). The carbon deposition was quantified by the CO_2 STY obtained in the O_2 oxidation step.

The performance of the reactor beds with different spatial structuring, built up with Ni/Zr@Zr catalyst or Fe/Zr@Zr-Ni@Zr bifunctional catalyst and Fe/Zr@Zr OSM, was examined during a prolonged CCAR process. A schematic representation of all reactor beds is displayed in Fig. 4. Prior to the CCAR experiments, all samples experienced a pretreatment of H_2 reduction and CO_2 re-oxidation: the samples were first reduced in a 180 mL min^{-1} flow of 10% H_2/Ar from room

temperature to 700°C at a rate of $10^\circ\text{C min}^{-1}$ and then the flow was switched to Ar for 5 min purging, after which CO_2 (180 mL min^{-1}) started flowing inside the reactor for 10 min in order to obtain an initial state of metallic Ni and Fe_3O_4 . Afterwards, the sample bed was heated to 750°C in Ar, and then 25 redox cycles were carried out with alternating 2 min reduction and 2 min re-oxidation sequences (always with 3 min of Ar purging in between) at a constant flow rate of 150 mL min^{-1} . The reducing feed was a mixture of $\text{CH}_4:\text{CO}_2:\text{O}_2:\text{Ar}$ (molar ratio of 1:1:0.2:0.2) and the oxidizing feed was 90% CO_2/Ar . The time-averaged space-time yield of CO ($\overline{\text{STY}}_{\text{CO}}$) was calculated based on the experimental CO space-time yield during the re-oxidation step of each cycle. After the CCAR experiments, carbon formation on the spent catalysts was checked through O_2 temperature programmed oxidation (TPO). Prior to running the TPO measurement, the sample was pretreated in a He stream at 350°C for 5 min and then cooled down to room temperature in He. Hereafter, the TPO was carried out by ramping the sample to 900°C at a rate of $10^\circ\text{C min}^{-1}$ in a 60 mL min^{-1} flow of 10% O_2/He . The CO_2 STY as a function of temperature was calculated to determine the carbon formation.

To simulate chemical looping operation in a permanent periodic regime based on the experimental CO space-time yield of the single-tubular reactor, a dynamic simulation for a multi-tubular reactor configuration was performed. Similar to a multi-column configuration in a pressure-swing adsorption (PSA) process, where each column is cycled between adsorption and regeneration, a multi-tubular reactor configuration allows continuous processing of a given feed stream. Such reactor consists of a set of fixed bed reactors, operated in parallel. The core of the simulation concept is that all single-tubular reactors are operated in chemical looping regime, but one after the other, i.e. with a delay relative to the preceding one. In this way, a redox cycle is established in each single-tubular reactor by switching the feed valves at discrete times, leading to an oscillating CO space-time yield and eventually generating a permanent periodic regime for the multi-tubular reactor concept. The oscillatory space-time yield (STY_{osc} , $\text{mol}_{\text{CO}} \text{ s}^{-1} \text{ kg}_{\text{Fe}_2\text{O}_3}^{-1}$) is defined by Eq. (11). It is determined by summing the contribution of each reactor (based on the single-tubular reactor experiment) at each time step and subsequent division by the number of reactors that are in material regeneration mode, n_{ox} , in order to take into account the utilization of a higher amount of active material.

$$\text{STY}_{\text{osc}} = \frac{\sum_{n_{\text{ox}}} F_{\text{CO}}}{n_{\text{ox}} * W_{\text{Fe}_2\text{O}_3}} = \frac{\sum_{n_{\text{ox}}} \text{STY}_{\text{CO}}}{n_{\text{ox}}} \quad (11)$$

where F_{CO} ($\text{mol}_{\text{CO}} \text{ s}^{-1}$) is the outlet molar flow rate of CO product and $W_{\text{Fe}_2\text{O}_3}$ ($\text{kg}_{\text{Fe}_2\text{O}_3}$) is the mass of Fe_2O_3 in the reactor. This value is used for calculating the $\overline{\text{STY}}_{\text{CO}}$ ($\text{mol}_{\text{CO}} \text{ s}^{-1} \text{ kg}_{\text{Fe}_2\text{O}_3}^{-1}$) which is the average value of the STY_{osc} in the permanent periodic regime.

3. Results and discussion

3.1. Material characterization

The morphological structure of the as-prepared materials was examined by STEM and EDX element mapping (Fig. 5). All materials show a core-shell structure. For Ni/Zr@Zr catalyst (Fig. 5a) and Fe/Zr@Zr OSM (Fig. 5b), the elemental distribution of Zr is composed of a big core with high intensity and a thin shell with low intensity. Ni or Fe ($\sim 20\text{--}30 \text{ nm}$) is distributed only in the interior of the Zr shell, consistent with our previous study [24]. The core-shell structure of Ni/Zr@Zr and Fe/Zr@Zr are equally retrieved in the data of EDX line-scan analysis recorded through the center of particle (Fig. S1, Supplementary materials). As observed, the trace signal starts and ends with Zr, while the Ni or Fe trace is located on the inside of the Zr trace, further confirming the core-shell structure. The STEM image for the Fe/Zr@Zr-Ni@Zr bifunctional catalyst (upper middle of Fig. 5c) confirms its

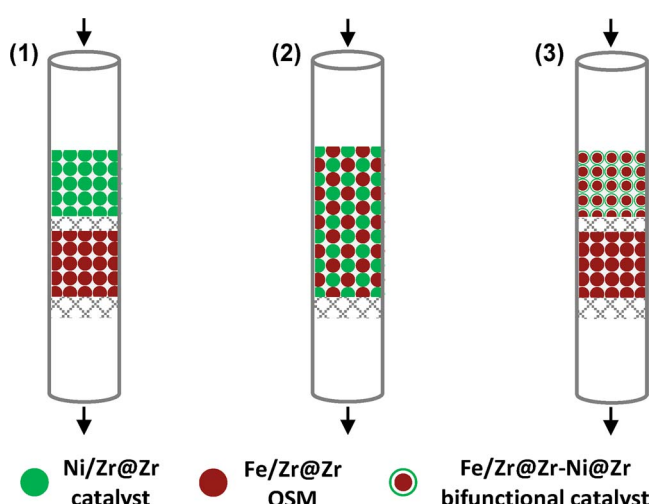


Fig. 4. Schematic representation of spatial structuring at the reactor bed scale using core-shell structured materials: (1) double-zone bed of Ni/Zr@Zr and Fe/Zr@Zr (labeled as NiFe_D1), (2) single-zone bed of Ni/Zr@Zr and Fe/Zr@Zr (NiFe_S2), (3) double-zone bed of Fe/Zr@Zr-Ni@Zr and Fe/Zr@Zr (BCFe_D3).

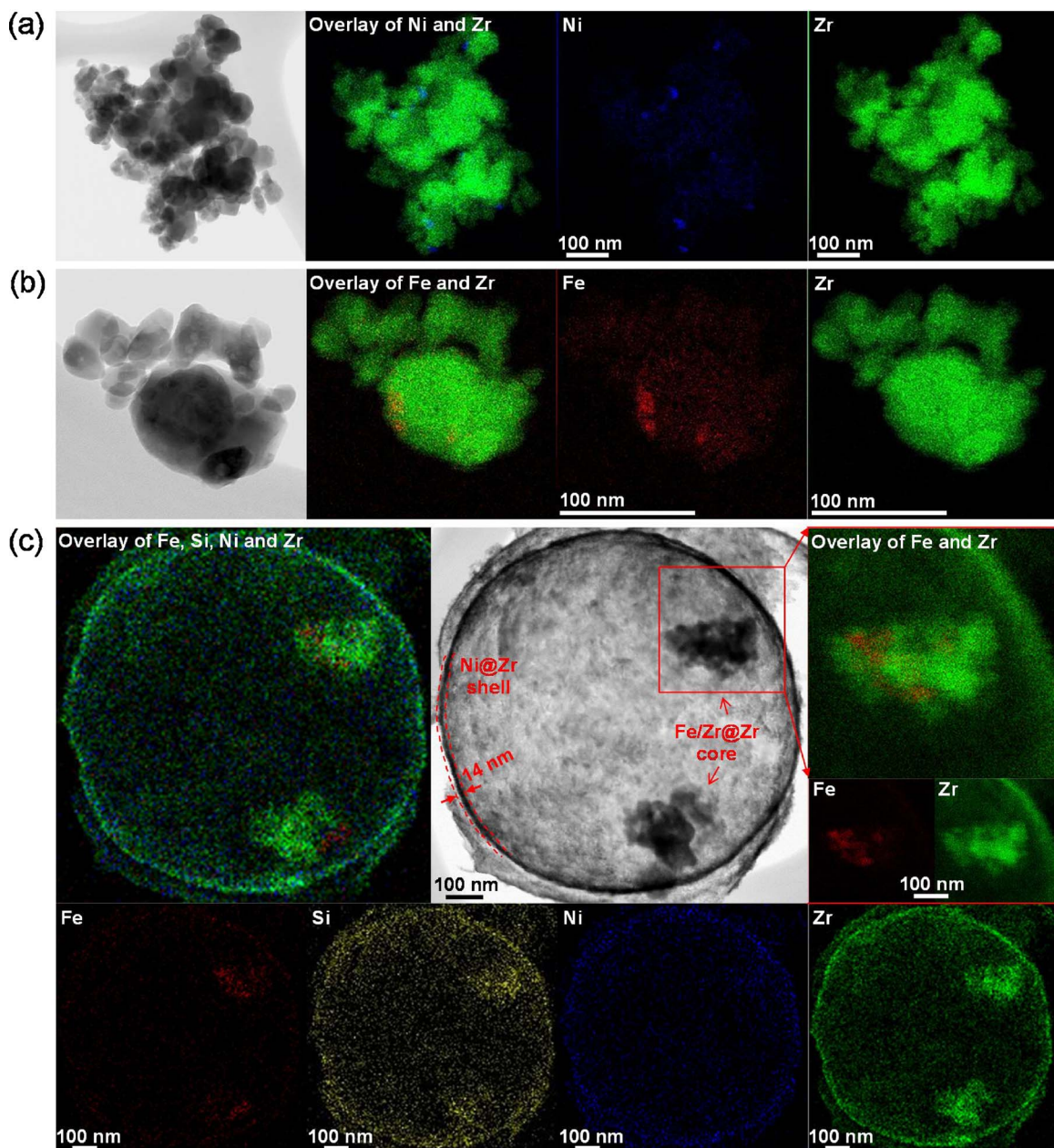


Fig. 5. STEM micrograph and EDX element mapping of Ni, Fe, Si and Zr, and the overlay mapping of these elements for fresh core-shell materials: (a) Ni/Zr@Zr catalyst, (b) Fe/Zr@Zr OSM and (c) Fe/Zr@Zr-Ni@Zr bifunctional catalyst.

eccentric core-shell structure, displaying a spherical shape, in which the core is completely or partially separated from the shell [45]. The former, acting as OSM, is the core-shell structured Fe/Zr@Zr confirmed by EDX-mapping of the zoomed red square area (upper right of Fig. 5c), and the latter, acting as reforming catalyst, is a thin shell (~14 nm) of Zr-coated Ni confirmed by the overlay EDX-mapping shown in the upper left of Fig. 5c. The absence of a substantial amount of Si is apparent from comparison of the STEM images and EDX-mappings of Fe/Zr@Zr-Si@Ni (Fig. S2) and Fe/Zr@Zr-Ni@Zr (Fig. 5c), confirming that most of the Si has been removed by NaOH extraction (the final step of the synthesis procedure, see Experimental Section 2.1.4). However, it is noted that trace amounts of Si are present in the Zr shell (see the EDX-mapping of Si in Fig. 5c), because of migration of Si from the bulk of the Si layer into the Zr shell during calcination (the third step of synthesis). This part of Si cannot be removed by NaOH extraction [49], but will continue to provide a stabilizing support for Ni in the shell. In addition, it can be observed that the particle size of Ni is very small (see

elemental distribution of Ni in the lower part of Fig. 5c). During the impregnation of Ni species on the SiO₂ surface (the second step of synthesis), Ni is highly dispersed on the surface of the SiO₂ sphere in the form of a thin and uniform layer, which can be observed by EDX-mapping of Fe/Zr@Zr-Si@Ni (Fig. S2).

The crystalline phases of the materials used in this study were determined from ex-situ XRD patterns (Fig. 6). The zirconia in fresh materials shows two main phases, monoclinic zirconia (m-ZrO₂, PDF: 83-0944) and tetragonal zirconia (t-ZrO₂, PDF: 80-2156), indicated either by diffraction peaks at 28.2°, 31.5° or a peak at 30.3°. According to previous work [24], the m-ZrO₂ phase pertains to the ZrO₂ support in the core, while the dominating phase in the shell is t-ZrO₂. Fe₂O₃ and NiO can be identified by the corresponding characteristic peaks at 33.2° (PDF: 33-0664) and at 37.3°, 43.3° (PDF: 47-1049), respectively. The other diffraction peaks originate from zirconia or the overlap of these crystalline phases. For Fe/Zr@Zr-Ni@Zr (Fig. 6d), no peak related to SiO₂ can be observed, indicating that only trace amounts of Si in a

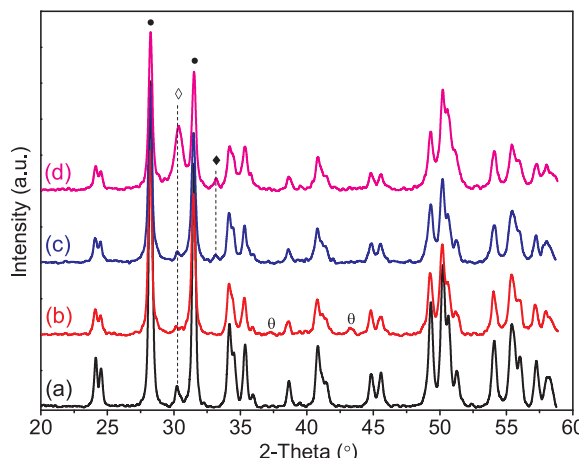


Fig. 6. XRD patterns of the as-prepared samples of (a) ZrO_2 support, (b) $\text{Ni}/\text{Zr@Zr}$ catalyst, (c) $\text{Fe}/\text{Zr@Zr}$ OSM and (d) $\text{Fe}/\text{Zr@Zr-Ni@Zr}$ bifunctional catalyst. Main peaks corresponding to crystalline phases were marked by the following symbols: (●) m-ZrO_2 , (○) t-ZrO_2 , (♦) Fe_2O_3 , (⊖) NiO .

nanocrystalline or amorphous form were left in the material after the extraction treatment with NaOH solution. XRD typically cannot detect an amorphous phase with a volume fraction of less than $\sim 5\%$ [52]. Furthermore, no obvious diffraction peak of NiO can be observed in the XRD pattern of $\text{Fe}/\text{Zr@Zr-Ni@Zr}$, confirming the high dispersion of nickel species in the outer Zr shell [53], as well as the small size of nickel particles (the minimum crystallite size for XRD detection is roughly 3 nm). This indicates that the ZrO_2 shell is able to prevent Ni particles from sintering during calcination and maintain their high dispersion. It is worth noting that the XRD peak of t-ZrO_2 for $\text{Fe}/\text{Zr@Zr-Ni@Zr}$ (Fig. 6d) has a more significant intensity compared to the one of its core material, $\text{Fe}/\text{Zr@Zr}$ (Fig. 6c), the reason being that the Si incorporated in the outer shell helps to stabilize t-ZrO_2 [49].

The actual Ni or Fe_2O_3 content, BET specific surface area (BET-SSA) and crystallite sizes of the main crystalline phases are reported in Table 1 for these materials. The amount of Fe_2O_3 is more than twice that of Ni in the $\text{Fe}/\text{Zr@Zr-Ni@Zr}$ bifunctional catalyst and as such similar to the loadings in a bifunctional bed composed of a physical mixture with $\text{Ni}/\text{Zr@Zr}$ catalyst and $\text{Fe}/\text{Zr@Zr}$ OSM. The BET-SSA of the core-shell materials are generally larger than that of the ZrO_2 support. As mentioned above, t-ZrO_2 is the dominating phase in the ZrO_2 shell, which could partially contribute to the large specific surface area of the materials [54,55]. The materials prepared following a similar synthesis method ($\text{Ni}/\text{Zr@Zr}$ and $\text{Fe}/\text{Zr@Zr}$) show a similar crystallite size and BET-SSA. The BET-SSA of $\text{Fe}/\text{Zr@Zr-Ni@Zr}$ is higher in correspondence with a smaller crystallite size of t-ZrO_2 in its outer shell [49]. However, the crystallite size of Fe_2O_3 in $\text{Fe}/\text{Zr@Zr-Ni@Zr}$ is much larger than in $\text{Fe}/\text{Zr@Zr}$, likely because it undergoes two calcinations (at $700\text{ }^\circ\text{C}$ for 4 h) during the synthesis of $\text{Fe}/\text{Zr@Zr-Ni@Zr}$. This could result in a lower activity of the bifunctional catalyst for CO_2

conversion to CO during the re-oxidation half-cycle of chemical looping (i.e. re-oxidation of Fe to Fe_3O_4 by CO_2).

3.2. Activity and stability of the reforming catalysts

Alternating deactivation and regeneration experiments were performed to examine the activity and stability of the two catalysts, $\text{Ni}/\text{Zr@Zr}$ and $\text{Fe}/\text{Zr@Zr-Ni@Zr}$, for methane dry reforming, and evaluated by CH_4 consumption rate and amount of carbon deposition (Fig. 7). The initial activity of $\text{Fe}/\text{Zr@Zr-Ni@Zr}$ is twice the one of $\text{Ni}/\text{Zr@Zr}$. Both decrease to about 50% of their initial level and then remain stable with time-on-stream, as seen in the left-hand graph of Fig. 7a. Although $\text{Fe}/\text{Zr@Zr-Ni@Zr}$ presents higher activity than $\text{Ni}/\text{Zr@Zr}$ after 4 h dry reforming, the amounts of carbon deposition are quite similar (left-hand graph of Fig. 7b), showing a better stability of the bifunctional catalyst. After regeneration, both $\text{Fe}/\text{Zr@Zr-Ni@Zr}$ and $\text{Ni}/\text{Zr@Zr}$ cannot completely regain the initial activity in the second dry reforming sequence (middle of Fig. 7a), implying that sintering of the Ni particles is another factor for deactivation under the present experimental conditions. However, the activity of $\text{Fe}/\text{Zr@Zr-Ni@Zr}$ (90% of the initial value) is better restored than the one of $\text{Ni}/\text{Zr@Zr}$ (60% of the initial value), indicating that the former has a higher ability to resist particle sintering. This is mainly because the bifunctional catalyst has a more stable structure, i.e. smaller Ni particles coated by a complete ZrO_2 shell, compared to $\text{Ni}/\text{Zr@Zr}$ (as shown by the STEM micrograph in Fig. 5).

In the third dry reforming sequence (right of Fig. 7a), both samples restore the same level of activity as in the second, meaning that sintering does not deteriorate the materials any further and the observed deactivation is mainly due to carbon deposition. It's worth noting that less carbon deposits are found on $\text{Fe}/\text{Zr@Zr-Ni@Zr}$ than on $\text{Ni}/\text{Zr@Zr}$ in the last two sequences (middle and right of Fig. 7b). This is ascribed to the formation of Ni-Fe alloy in the bifunctional catalyst during reduction, which contributes to eliminate the carbon deposition [13]. The Ni-Fe alloy formation in the $\text{Fe}/\text{Zr@Zr-Ni@Zr}$ bifunctional catalyst under reduction environment was confirmed by in-situ XRD during H_2 -TPR (Fig. S3), where a shoulder diffraction peak at an angle of 44.22° , corresponding to a Ni-Fe alloy peak [2,13,35], appears from $500\text{ }^\circ\text{C}$ and steadily gains intensity with increasing temperature. The alloy formation results from the migration of uncoated Fe_2O_3 particles from the $\text{Fe}/\text{Zr@Zr}$ core to the Ni shell. The migration of active metal particles under reduction environment during methane reforming has been reported before [8,56]. In particular, the carbon formation on $\text{Fe}/\text{Zr@Zr-Ni@Zr}$ even decreases in the third sequence compared to that in the second sequence, probably because more Ni-Fe alloy is formed with the proceeding deactivation/regeneration experiments. Therefore, both the structural stability and carbon resistance are responsible for maintaining the good performance of the $\text{Fe}/\text{Zr@Zr-Ni@Zr}$ bifunctional catalyst in methane dry reforming as well as in chemical looping.

Table 1
Material properties.

Material	Loading ^a (wt%)		BET-SSA ($\text{m}^2 \text{g}^{-1}$)	Crystallite size ^b (nm)			
	Ni	Fe_2O_3		m-ZrO ₂	t-ZrO ₂	NiO	Fe_2O_3
ZrO_2 support	–	–	8.7 ± 1.0	55.2 ± 1.1	30.2 ± 4.1	–	–
$\text{Ni}/\text{Zr@Zr}$	1.95	–	13.7 ± 2.3	50.0 ± 1.4	55.8 ± 4.0	27.4 ± 3.0	–
$\text{Fe}/\text{Zr@Zr}$	–	4.5	15.3 ± 1.1	45.2 ± 1.3	52.8 ± 4.7	–	27.9 ± 4.2
$\text{Fe}/\text{Zr@Zr-Ni@Zr}$	1.38	3.92	29.2 ± 2.0	46.4 ± 1.5	19.2 ± 0.7	–	56.3 ± 3.4

^a The actual loading of Ni and Fe_2O_3 was determined by ICP.

^b The crystallite size of the crystalline phase in as-prepared samples was calculated from their main XRD peak and the error range was determined as the standard error of Gaussian fitting.

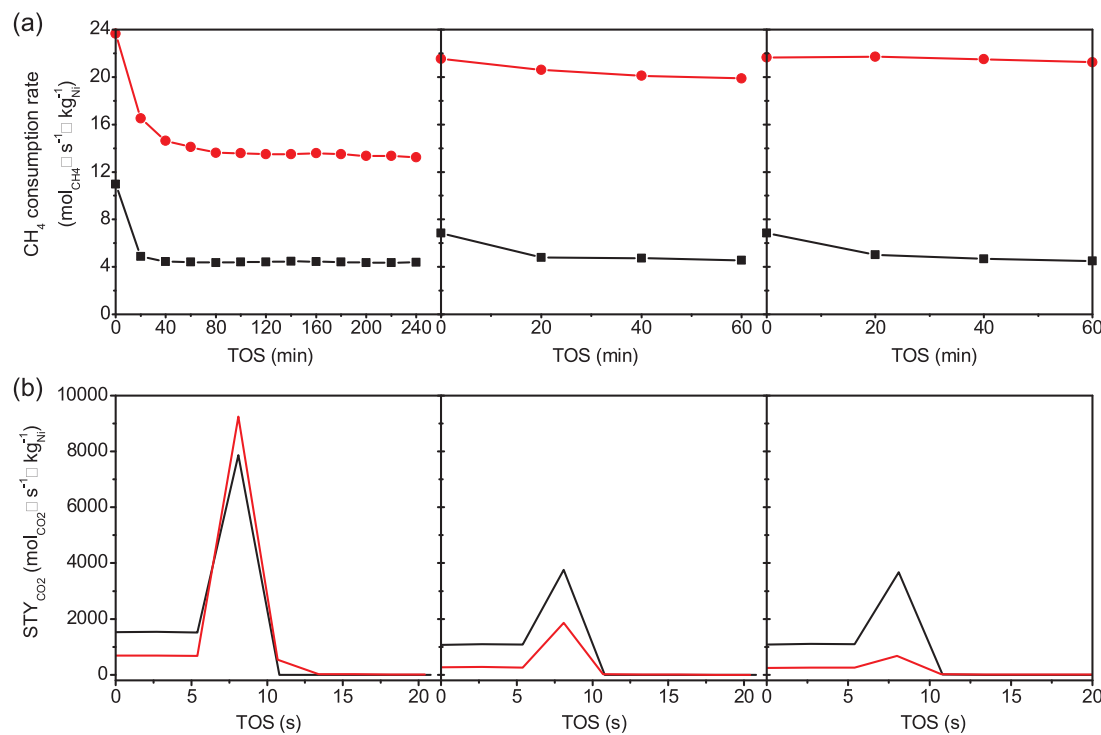


Fig. 7. (a) CH₄ consumption rate during dry reforming of a CH₄:CO₂ (1:0.8) mixture over Ni/Zr@Zr (■) and Fe/Zr@Zr-Ni@Zr (●); (b) CO₂ space-time yield upon O₂ oxidation of deposited carbon on spent samples of Ni/Zr@Zr (—) and Fe/Zr@Zr-Ni@Zr (—). Three deactivation/regeneration sequences were performed at 750 °C: first dry reforming test, TOS = 240 min; second and third tests, TOS = 60 min. O₂ oxidation and H₂ reduction: each 10 min.

3.3. Redox behavior

As a means for identifying the evolution of crystal phases in the core-shell structured materials during redox reactions, four samples were subjected to three consecutive redox cycles at 750 °C, while being monitored with in-situ XRD (Fig. 8). Some changes in background intensity appear because of the effect of different atmospheres (H₂, CO₂ and He) on X-ray scattering. For Ni/Zr@Zr (Fig. 8a), NiO is rapidly reduced to metallic Ni after contact with H₂ in the first cycle, whereafter the metallic Ni peak remains almost constant. No obvious NiO peak can be observed in the following two cycles, demonstrating that the metallic Ni phase is stable in repeating redox cycles. For Fe/Zr@Zr (Fig. 8b), in the initial H₂ reduction the FeO diffraction first gains intensity at the expense of Fe₂O₃ and then quickly gives way to Fe which directly transforms to Fe₃O₄ in the following CO₂ re-oxidation. In the second and third cycle, the redox behavior of the iron system follows the consecutive transitions Fe₃O₄ → FeO → Fe in the reduction half-cycle and the direct transformation Fe → Fe₃O₄ in the re-oxidation half-cycle. The direct transformation of metallic Fe to Fe₃O₄ during the re-oxidation half-cycle contributes to achieve the complete regeneration of Fe₃O₄ in a short time (such as 2 min in the present experiments), which is important to keep up the high oxygen storage capacity of the OSM in the CCAR process.

For the mixture sample of Ni/Zr@Zr and Fe/Zr@Zr (Fig. 8c), NiO immediately transforms to Ni in the first H₂ reduction half-cycle, while Fe₂O₃ is quickly reduced to Fe with a short-lived transition of FeO. At the same time, the Ni-Fe alloy is formed, leading to the co-existence of Ni, Fe and Ni-Fe alloy in the Ni/Zr@Zr and Fe/Zr@Zr mixture during the reduction half-cycle of CCAR. During re-oxidation, the Ni-Fe alloy peak disappears and Fe is re-oxidized to Fe₃O₄, while the Ni peak remains constant and no significant NiO is observed, indicating that Ni and Fe₃O₄ are formed as dominant phases in the physical mixture after 2 min re-oxidation by CO₂ at 750 °C. The above crystal phases of Ni and Fe species formed during redox cycling can be further determined by plotting the XRD peaks upon the 20 range of 42.5°–46.5° at the selected

timeline of the first redox cycle, as shown in Fig. S4a. The change in crystal phases of the Fe/Zr@Zr-Ni@Zr bifunctional catalyst during redox reactions (Fig. 8d) approximately follows the same evolution as for the mixture sample of Ni/Zr@Zr and Fe/Zr@Zr. Even though the presence of NiO and Ni are difficult to be observed on the in-situ XRD pattern, the formation of the Ni-Fe alloy during H₂ reduction is clearly monitored (see Fig. S4b), due to the large particle size of the alloyed species, which results in an obvious Ni-Fe alloy diffraction.

Because the Ni species of the Fe/Zr@Zr-Ni@Zr bifunctional catalyst are not observable with XRD, the evolution of the oxidation state of Ni in Fe/Zr@Zr-Ni@Zr was further monitored by performing XPS measurements at different stages, i.e. as prepared, reduced and spent after 25 CCAR cycles. The XPS wide scans are shown in Fig. S5 and contain photoemission lines for O, C, Zr, Ni and Fe, with traces of Si. Fig. 9 displays the detail photoemission signal of the Ni2p_{3/2} peak. The signal for the as prepared sample consists of a broad Ni2p_{3/2} peak, corresponding to Ni²⁺ at ~854 eV (15 at% of the main Ni peak) and Ni³⁺ at ~856–857 eV (85 at%), followed by a multiplet peak at ~861 eV [57]. The first Ni²⁺ contribution can be ascribed to NiO, the Ni³⁺ to Ni₂O₃ [51,58]. The co-existence of NiO and Ni₂O₃ phases in a NiO-ZrO₂ system has been described in previous studies [58–60]. Ni₂O₃ is believed not only to serve as a matrix that decreases the Ni atoms agglomeration [61], but also to play an important role in methane oxidation, owing to its oxygen storage property [62–64]. Hence, the presence of the surface Ni₂O₃ phase in the bifunctional catalyst could be favorable to maintain its high stability and reactivity during the CCAR process. After reduction, a new contribution appeared at ~852.5 eV. The latter can be due to metal-like Ni species, or may originate from the Ni-Fe alloy. According to previous XPS observations on Ni-Fe alloys [51,65–67], the alloying process may shift Ni° over +0.3 to +0.5 eV. Curve fitting of the Ni2p_{3/2} signal indicates that in reduced state ~21 at % of Ni was metal- or alloy-linked, while 29 at% is Ni²⁺ and 50 at% in Ni³⁺ state. After CCAR reaction, the Ni2p_{3/2} photoline resembled the fresh one, with more Ni³⁺ than Ni²⁺, 84 vs. 16 at%, indicating that the surface metallic Ni in Fe/Zr@Zr-Ni@Zr can be oxidized by CO₂ in the

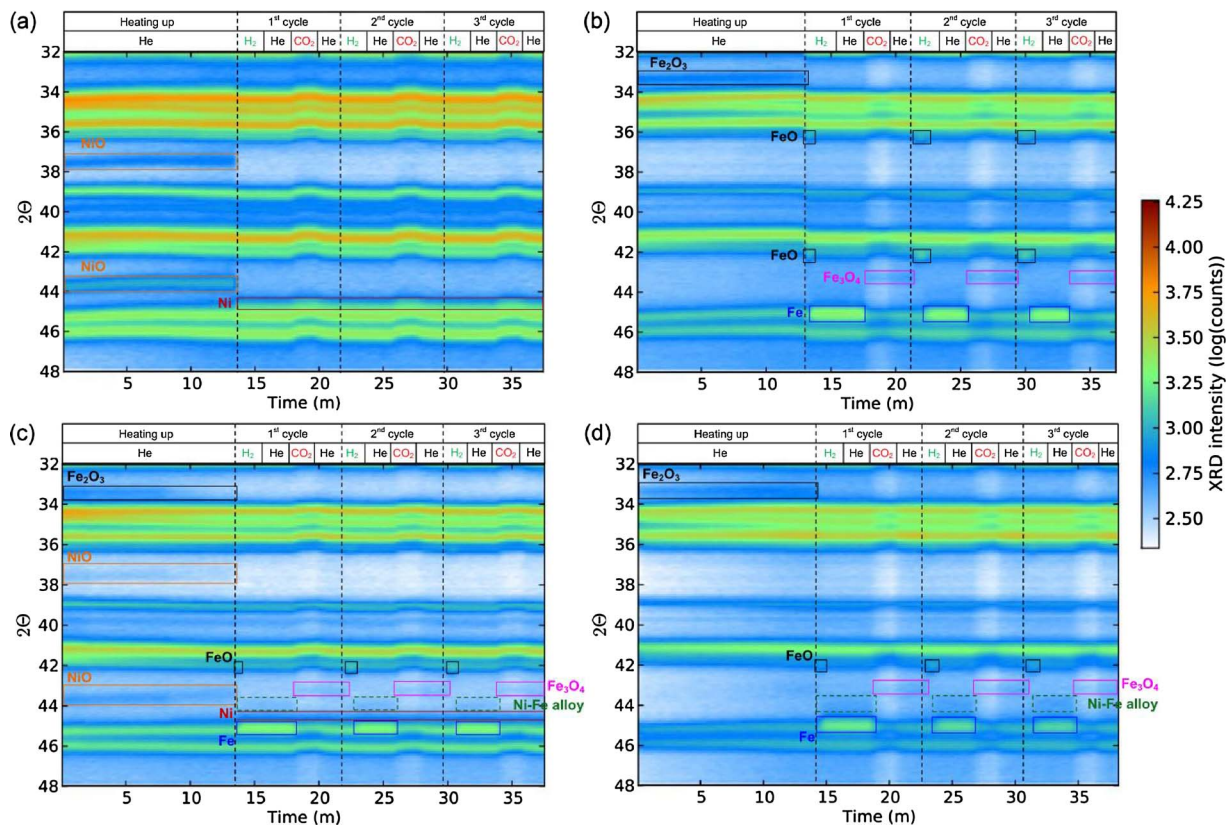


Fig. 8. 2D in-situ XRD patterns recorded during isothermal redox cycles at 750 °C for (a) Ni/Zr@Zr catalyst, (b) Fe/Zr@Zr OSM, (c) a physical mixture of Ni/Zr@Zr and Fe/Zr@Zr, and (d) Fe/Zr@Zr-Ni@Zr bifunctional catalyst. Each cycle (8 min) comprises alternate pulses of 2 min H₂ (5% in He), 2 min He, 2 min CO₂ and 2 min He. All gas flow rates were 60 mL min⁻¹.

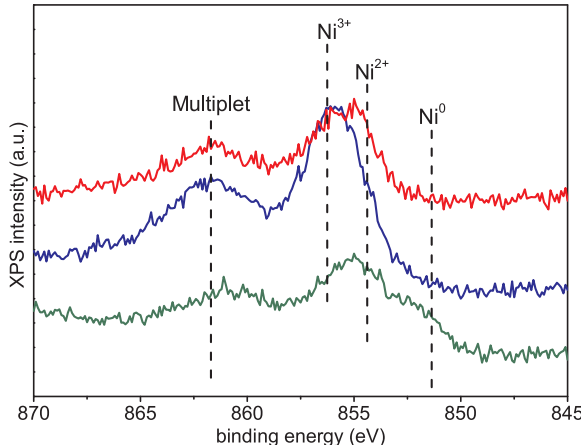


Fig. 9. XPS detail windows of the Ni2p_{3/2} photoline for the Fe/Zr@Zr-Ni@Zr bifunctional catalyst in three different states: as prepared (blue line); reduced (green line); spent after 25 CCAR cycles (red line). (For interpretation of the references to colour in this figure legend, the reader is referred to the web version of this article.)

re-oxidation half-cycle. This oxidation is probably caused by O species, originating from the dissociation of CO₂ on the Ni-ZrO₂ boundary, promoted through the interaction between Ni and t-ZrO₂ [68–71].

3.4. Catalyst-assisted chemical looping auto-thermal dry reforming (CCAR)

3.4.1. Optimal spatial structuring at reactor bed scale

A complete CCAR process includes two half-cycles: catalytic auto-thermal dry reforming of methane over Ni and the reduction of Fe₃O₄ by syngas (reduction half-cycle), followed by re-oxidation of Fe by CO₂ accompanied with CO production (re-oxidation half-cycle). To investigate the effect of spatial structuring at reactor bed scale on the

process efficiency, i.e. CH₄ conversion and CO₂ utilization, the activity of different reactor bed configurations was assessed. 25 cycles of CCAR at 750 °C were performed over a double-zone Ni/Zr@Zr catalyst and Fe/Zr@Zr OSM bed (abbreviated as NiFe_D1), a single-zone bed with a mixture of Ni/Zr@Zr and Fe/Zr@Zr (NiFe_S2), as well as over a double-zone Fe/Zr@Zr-Ni@Zr bifunctional catalyst and Fe/Zr@Zr OSM bed (BCFe_D3) (Fig. 4).

Fig. 10 displays an example of the space-time yield of products vs. time on stream in the CCAR process for NiFe_D1 and NiFe_S2 to understand the differences in activity between double- and single-zone reactor bed configurations.

The activity of the two configurations in the reduction half-cycle is similar: when fed into the reactor, CH₄, CO₂ and O₂ are immediately converted to syngas with a H₂:CO ratio higher than 1 initially. Within the first 20 s, the produced syngas rapidly decreases due to the reduction of Fe₃O₄ into metallic Fe. The CO₂ STY on the other hand exhibits a transient behavior, because of the water-gas shift reaction (CO + H₂O → CO₂ + H₂). The O₂ conversion is always 100% in the present conditions. Towards the end of the reduction half-cycle, the dominating reaction is methane dry reforming, yielding syngas with a H₂:CO ratio of unity, accompanied by some methane combustion into CO₂ and H₂O. In the re-oxidation half-cycle, CO₂ is fast converted to CO through the re-oxidation of Fe into Fe₃O₄. The STY of CO production therefore shows a sharp peak in the first 20 s and then steadily decreases towards zero, showing that the majority of Fe₃O₄ can be regenerated in 20 s, in agreement with the duration of syngas consumption for Fe₃O₄ reduction in the reduction half-cycle. However, the amount of CO production in the NiFe_D1 bed is higher than that in NiFe_S2, indicating a higher capacity of the former for CO₂ utilization.

In general, the amount of CO₂ conversion to CO in the re-oxidation half-cycle depends on the amount of metallic Fe generated from the Fe₃O₄ reduction in the reduction half-cycle. Fig. 11 presents schematically the evolution of gas and solid species during the reduction half-

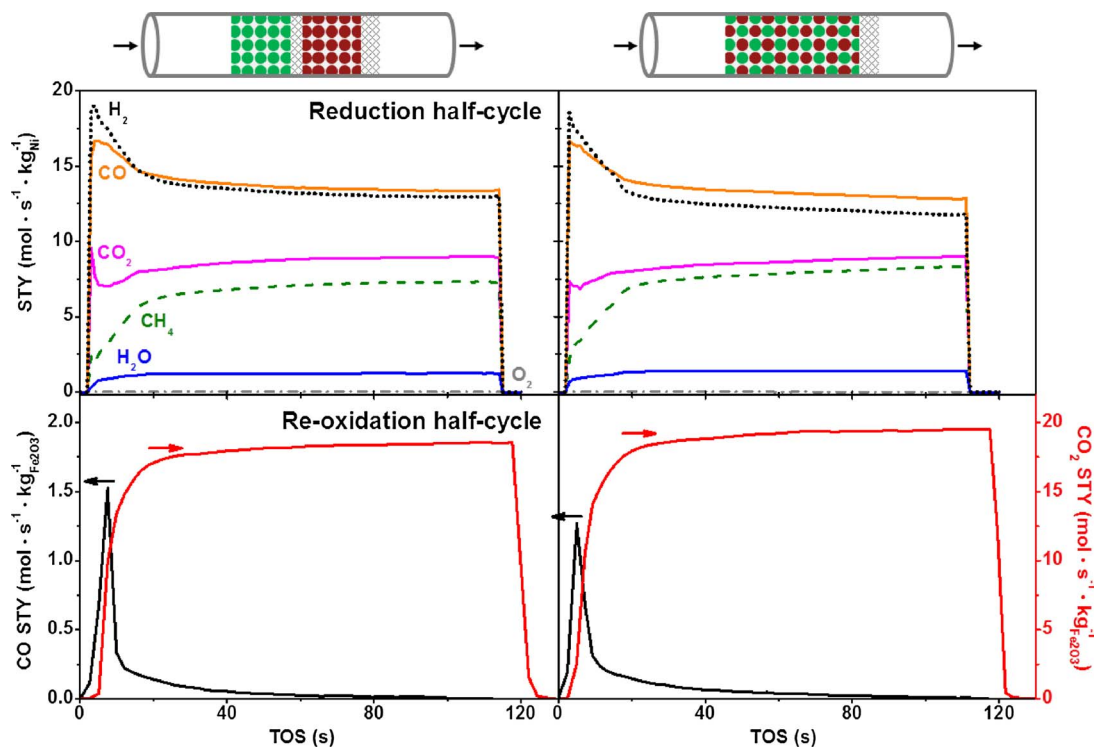


Fig. 10. Reactivity of NiFe_D1 (left figure) and NiFe_S2 (right figure) during the CCAR process at 750 °C. Reduction half-cycle (upper figure): space-time yields of CH₄, CO₂, O₂, CO, H₂ and H₂O in the product stream vs. time on stream during catalytic auto-thermal dry reforming of CH₄ and Fe/Zr@Zr OSM reduction (reactant: mixture of CH₄:CO₂:O₂ = 1:1:0.2, 150 mL min⁻¹); Re-oxidation half-cycle (lower figure): space-time yield of CO and CO₂ during re-oxidation of Fe to Fe₃O₄ (reactant: 90% CO₂/Ar, 150 mL min⁻¹).

cycle. For the double-zone catalyst and OSM bed, the mixture of CH₄, CO₂ and O₂ is first converted to syngas over Ni in the first zone, and then syngas flows into the second zone to reduce Fe₃O₄ completely. Thus, the complete oxygen storage capacity of the OSM is available to be used in the re-oxidation half-cycle. For the single-zone bed, the feed gas contacts with a mixture of catalyst and OSM distributed over the whole reactor bed. The syngas production is limited due to the lack of Ni catalyst in the front region of the reactor bed, and hence Fe₃O₄ is difficult to reduce under the dominant presence of oxidizing gas (CO₂, H₂O and O₂) over reducing gas (CO and H₂). With increasing reactor coordinate, more Ni is involved and the syngas yield raises, accordingly

increasing the extent of Fe₃O₄ reduction. Finally, Ni, Fe and Ni-Fe alloy co-exist in the bed under a high concentration of reducing gases. Both the inadequate Fe₃O₄ reduction and Ni-Fe alloy formation (see Fig. 8c), result in incomplete utilization of the oxygen storage capacity of the OSM in the re-oxidation half-cycle [2], when using a single-zone bed. The above elaborations are supported by a thermodynamic analysis on the reaction equilibrium of the gas and solid phases (Fig. S6). Ni remains present as metal throughout the entire range of (CO + H₂)/(CO₂ + H₂O) ratios. However, the state of the Fe species strongly depends on the ratio between reducing and oxidizing gases, while the latter depends on CH₄ and CO₂ conversion. For low conversions, the

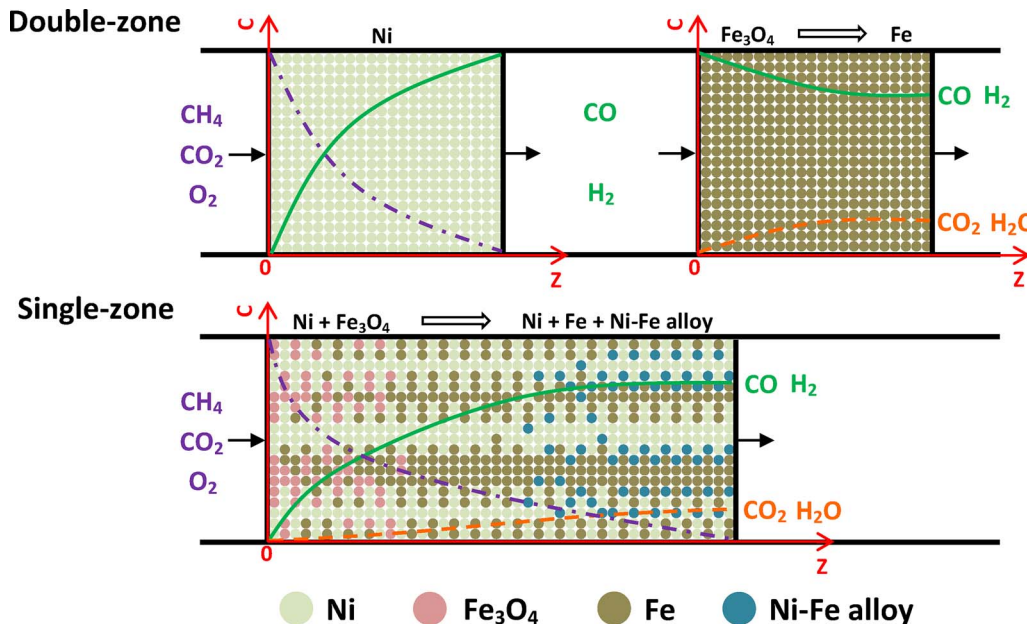


Fig. 11. Schematic representation of the evolution of gas (CH₄, CO₂, O₂, CO, H₂ and H₂O) and solid (Ni, Fe₃O₄, Fe and Ni-Fe alloy) species during the reduction half-cycle of the CCAR process in the double- and single-zone reactor bed configuration. The coordinate graph (red axes) shows the concentration (C) of the feed gas (CH₄ + CO₂ + O₂, purple line) as well as the produced reducing gas (CO + H₂, green line) and oxidizing gas (CO₂ + H₂O, blue line) vs. the reactor coordinate (Z). (For interpretation of the references to colour in this figure legend, the reader is referred to the web version of this article.)

$(CO + H_2)/(CO_2 + H_2O)$ ratio remains equally low and reduction of Fe_3O_4 is limited. Only for higher conversions, reduction of Fe_3O_4 to Fe is enabled by a higher $(CO + H_2)/(CO_2 + H_2O)$ ratio. Subsequently, metallic Ni in contact with Fe forms alloy under the high $(CO + H_2)/(CO_2 + H_2O)$ ratio (originating from the high conversion of CH_4 and CO_2 , which can be obtained in the end region of the single-zone bed). These phenomena support the evolution of gas and solid species along the reactor coordinate in the single-zone bed during the reduction half-cycle of CCAR. As for the double-zone bed, the CH_4 and CO_2 conversion respectively reach 70% and 60% during the reduction half-cycle in the Ni catalyst zone under the present experimental conditions, which can ensure the complete reduction of the OSM based on the thermodynamic analysis.

Compared with the single-zone bed, the double-zone bed can adequately produce syngas by catalyzing methane auto-thermal dry reforming in the first zone, which afterwards flows into the second zone to reduce the OSM completely. Hence, the double-zone catalyst and OSM bed configuration keeps up the high oxygen storage capacity for CO_2 utilization. Now, it was shown in §3.2 that the $Fe/Zr@Zr-Ni@Zr$ bifunctional catalyst has a higher activity and stability for catalyzing CH_4 conversion during dry reforming than the $Ni/Zr@Zr$ catalyst (see Fig. 7). Therefore, a double-zone $Fe/Zr@Zr-Ni@Zr$ bifunctional catalyst and $Fe/Zr@Zr$ OSM bed (BCFe-D3) is constructed to combine both advantages (Fig. 12a). The $Fe/Zr@Zr-Ni@Zr$ in the upper zone is used to achieve higher conversion of CH_4 , CO_2 and O_2 to syngas in the reduction half-cycle, to ensure complete reduction of the OSM. On the other hand, the oxygen storage capacity is provided by the original $Fe/Zr@Zr$ OSM in the second zone, which in combination with the $Fe/Zr@Zr$ core in the bifunctional catalyst (Fig. S7), leads to a higher CO production during the re-oxidation half-cycle (Fig. 12b).

Comparison of the CO time-averaged space-time yields (\overline{STY}) in the re-oxidation half-cycle (Fig. 13) shows all reactor beds can provide a stable CO yield during 25 cycles. The CO \overline{STY} of the reactor beds follows the order: BCFe-D3 > NiFe-D1 > NiFe-S2. Clearly, the double-zone $Fe/Zr@Zr-Ni@Zr$ bifunctional catalyst and $Fe/Zr@Zr$ OSM bed provides the optimal spatial structuring at reactor bed scale for CH_4 conversion and CO_2 utilization during catalyst-assisted chemical looping auto-thermal dry reforming.

3.4.2. Optimal spatial structuring at pellet scale

All investigated reactor beds allow a stable \overline{STY} of CO during 25 redox cycles of CCAR. The O_2 -TPO profile shows no significant carbon

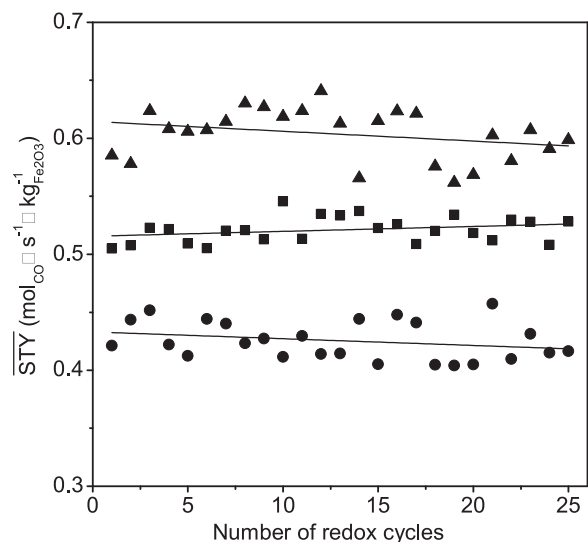


Fig. 13. Time-averaged space-time yield (\overline{STY}) of CO during a 2 min re-oxidation half-cycle with 90% CO_2/Ar (150 $mL\ min^{-1}$) in the CCAR process at 750 °C in different reactor beds: NiFe-D1 (square symbol), NiFe-S2 (spherical symbol) and BCFe-D3 (triangle symbol). The solid lines represent the trends of CO \overline{STY} over 25 cycles calculated by linear fitting to the values of \overline{STY} .

formation on the spent catalysts (Fig. S8), which illustrates the advantages of CCAR process mentioned above, i.e. the presence of O_2 helps to eliminate carbon formation in the reduction half-cycle and the deposited carbon can be further removed by reacting with CO_2 during the re-oxidation half-cycle [72]. Furthermore, analysis of the C1s photoemission peak in the XPS wide scans on $Fe/Zr@Zr-Ni@Zr$ (Fig. S5) shows that the amount of carbon present on the surface remained constant for all three states of the bifunctional catalyst, further indicating no carbon deposition on $Fe/Zr@Zr-Ni@Zr$ after 25 CCAR cycles.

Thus, the effect of the spatial structuring at the pellet scale on the stability of the materials was evaluated by the characterization of the crystal structure and morphology of the spent samples. Fig. 14 shows the changes in crystallite size of the main crystalline phases for the materials from different reactor beds, calculated based on their main XRD diffraction peaks (as seen in Figs. 6 and S9). The crystallite size of

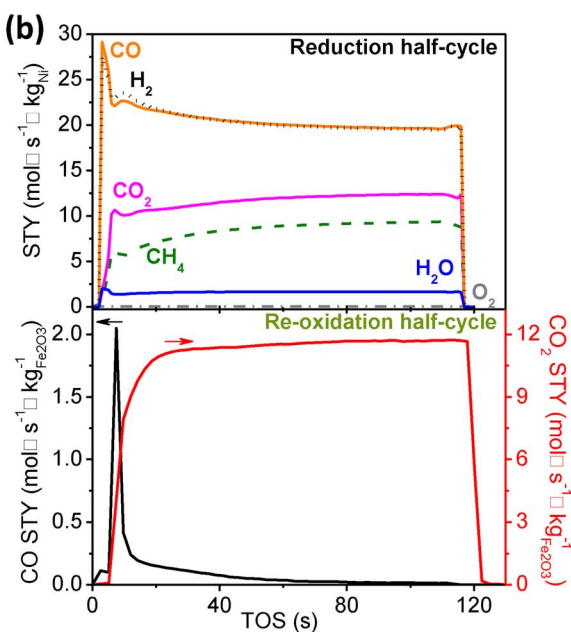
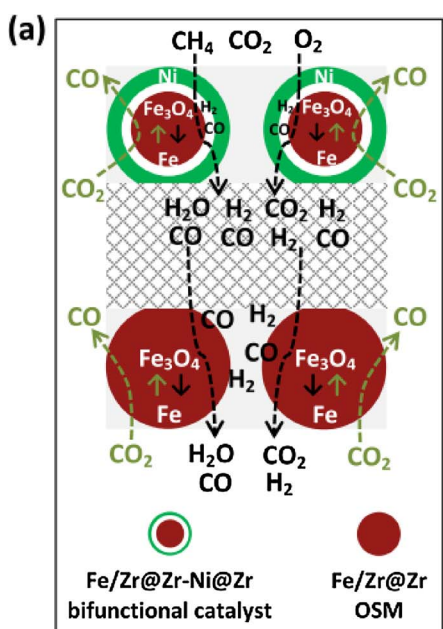


Fig. 12. (a) Schematic representation of the operating mode of the double-zone $Fe/Zr@Zr-Ni@Zr$ and $Fe/Zr@Zr$ bed (BCFe-D3) during catalyst-assisted chemical looping auto-thermal dry reforming. The black and green arrows represent the reaction routes in the reduction and re-oxidation half-cycle, respectively. (b) An example of the reactivity of the BCFe-D3 bed in the CCAR process: space-time yields of CH_4 , CO_2 , O_2 , CO , H_2 and H_2O in the product stream vs. time on stream during the reduction half-cycle (upper figure) and space-time yield of CO and CO_2 during the re-oxidation half-cycle (lower figure). (For interpretation of the references to colour in this figure legend, the reader is referred to the web version of this article.)

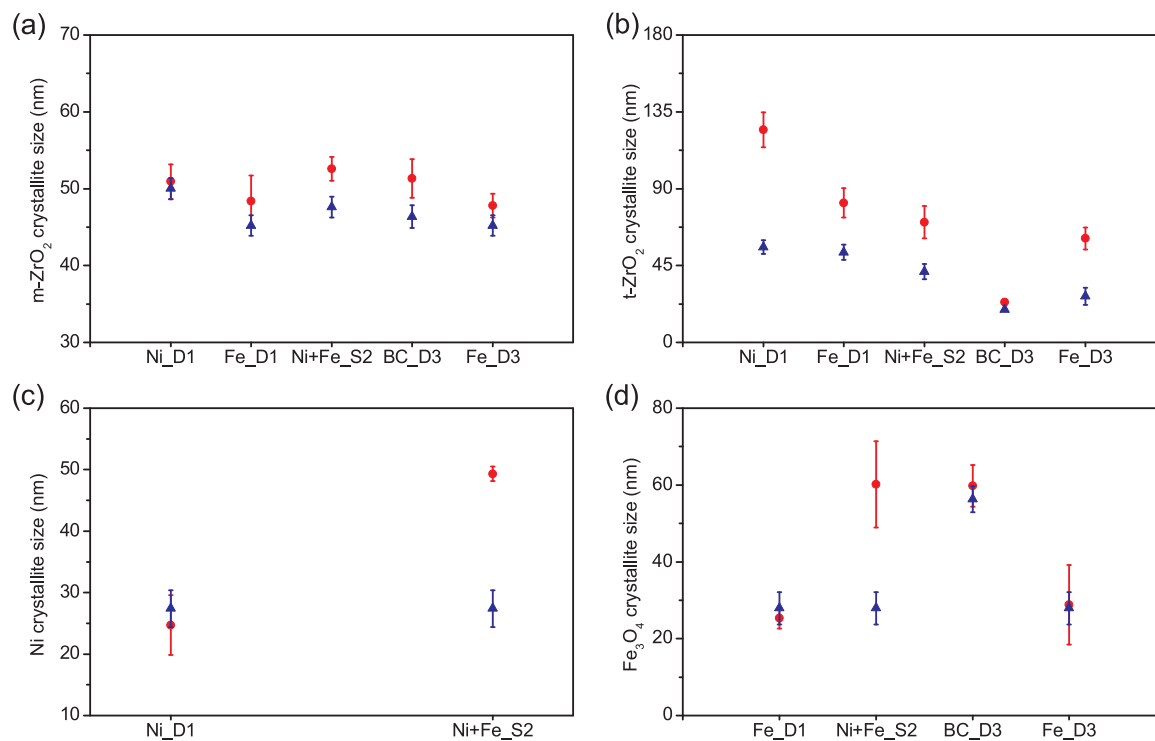


Fig. 14. Crystallite size of m-ZrO₂ (a), t-ZrO₂ (b), Ni (c) and Fe₃O₄ (d) in fresh (▲) and spent (●) samples after 25 CCAR cycles of Ni/Zr@Zr catalyst (abbreviated as Ni), Fe/Zr@Zr OSM (Fe), physical mixture of Ni/Zr@Zr and Fe/Zr@Zr (Ni + Fe) as well as Fe/Zr@Zr-Ni@Zr bifunctional catalyst (BC) used in different reactor beds: NiFe_D1 (abbreviated as D1), NiFe_S2 (S2) and BCFe_D3 (D3). The label for a sample, for example, Ni_D1 represents the spent sample of Ni/Zr@Zr in the top zone of the NiFe_D1 reactor bed. Crystallite size and error bar were calculated based on XRD data by Gaussian fitting.

m-ZrO₂ (the dominating phase of the ZrO₂ support) in all samples remains constant (Fig. 14a), indicating that the ZrO₂ support is stable during redox cycling. The crystallite size of t-ZrO₂ (Fig. 14b), the dominating phase of the ZrO₂ shell, does not show obvious change in Fe/Zr@Zr-Ni@Zr bifunctional catalyst, confirming that it is a very stable shell. However, the crystallite sizes of t-ZrO₂ in the spent Ni/Zr@Zr and Fe/Zr@Zr samples are significantly larger than in their fresh counterparts, showing sintering of the shell. Comparing the changes in BET-SSA of the mixed Ni/Zr@Zr and Fe/Zr@Zr sample with Fe/Zr@Zr-Ni@Zr (Fig. S10), the lower decrease in surface area of the latter further confirms its more stable ZrO₂-shell. The crystallite sizes of Ni (Fig. 14c) and Fe₃O₄ (Fig. 14d) remain constant in the samples from the double-zone Ni/Zr@Zr and Fe/Zr@Zr bed, but show an obvious increase for the mixed sample from the single-zone bed. This indicates that the formation of Ni-Fe alloy during redox cycles in the single-zone bed (confirmed by in-situ XRD, see Figs. 8c and S4a) facilitates particle sintering. In addition, the Ni diffraction peak is still not observed in the XRD pattern of the Fe/Zr@Zr-Ni@Zr bifunctional catalyst after 25 CCAR cycles (Fig. S9c), implying that the Ni particles do not suffer from sintering. The crystallite size of Fe₃O₄ in the bifunctional catalyst only slightly increases after 25 cycles (Fig. 14d), even though the Ni-Fe alloy is also formed (see Figs. 8d and S4b). This demonstrates that the eccentric core-shell structure of the bifunctional catalyst, provided with two layers of ZrO₂ coating – one from the Fe OSM core and another from the Ni catalyst shell – contributes to suppress to some extent the occurrence of particle migration during the Ni-Fe alloy formation.

The morphological structure of the spent materials from different reactor beds after 25 CCAR cycling is shown in Fig. 15. Comparison with the fresh samples shown in Fig. 5a and b, indicates that while particle sintering occurs during CCAR cycling in both the double- (Fig. 15a) and single-zone (Fig. 15b) bed of Ni/Zr@Zr and Fe/Zr@Zr, the sintering of Ni and Fe particles in the latter (Ni: ~30–85 nm, Fe: ~60–120 nm) is more pronounced than in the former (Ni: ~20–30 nm, Fe: ~50–60 nm), in agreement with the results displayed in Fig. 14c.

and d. For the Fe/Zr@Zr-Ni@Zr bifunctional catalyst (Fig. 15c), its eccentric core-shell structure has good thermal stability without showing collapse or aggregation during prolonged CCAR. The Fe/Zr@Zr OSM core is still core-shell structured and Ni is still encapsulated by the outer Zr-shell that remains unchanged in morphology, particle size and thickness (~11–12 nm). Compared to the fresh sample (Fig. 5c), the particle size of Ni in the spent sample shows a slight increasing due to sintering, while still being smaller than ~5–8 nm. Additionally, the enrichment of Fe in the outer shell, where Ni resides, further confirms the formation of Ni-Fe alloy in the bifunctional catalyst during redox cycling.

4. Conclusions

A combined impregnation and nanocoating method was used to synthesize core-shell structured materials, such as Ni/Zr@Zr catalyst, Fe/Zr@Zr oxygen storage material and Fe/Zr@Zr-Ni@Zr bifunctional catalyst. These materials were employed to construct two reactor bed configurations, based on the concept of double- and single-zone distribution of catalyst and OSM, to investigate the effect of spatial structuring at reactor bed scale on the process efficiency for CCAR. In all reactor beds, the mixture of CH₄:CO₂:O₂ (1:1:0.2) is converted into syngas with a unity H₂:CO ratio at 750 °C in the reduction half-cycle, and pure CO is produced via CO₂ utilization in the re-oxidation half-cycle. The double- and single-zone Ni/Zr@Zr catalyst and Fe/Zr@Zr OSM bed show a similar activity in the reduction half-cycle. Nevertheless, the former has a higher CO yield in the re-oxidation half-cycle owing to the more complete reduction of the OSM by the syngas, generated in sufficient amount in the first reactor zone, as well as to the absence of Ni-Fe alloy formation.

A deactivation/regeneration experiment for catalysts and characterization of spent samples after 25 cycles of CCAR from different reactor beds were performed to study the effect of spatial structuring at the pellet scale upon the stability of the materials. The bifunctional

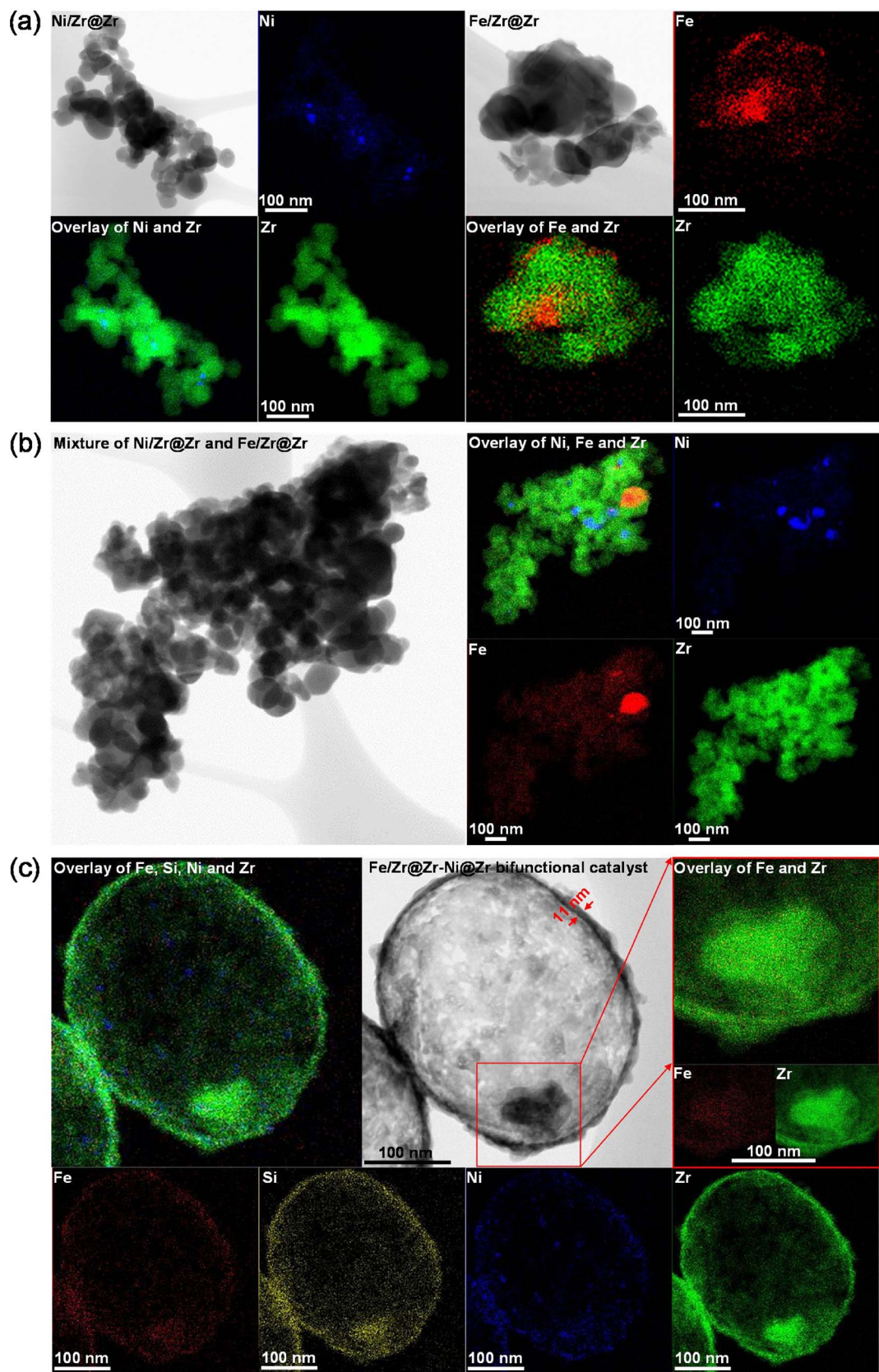


Fig. 15. STEM micrographs and EDX element mappings for the spent samples after 25 cycles of CCAR of Ni/Zr@Zr catalyst, Fe/Zr@Zr OSM, mixture of Ni/Zr@Zr and Fe/Zr@Zr, as well as Fe/Zr@Zr-Ni@Zr bifunctional catalyst from different reactor beds: NiFe_D1 bed (a), NiFe_S2 (b) and BCFe_D3 (c).

catalyst has higher methane dry reforming activity and ability of carbon resistance than the Ni/Zr@Zr catalyst due to a smaller Ni particle size (< 3 nm) and a positive effect of Fe addition. Comparison of the structure of the as-prepared and spent materials after 25 cycles of CCAR in different reactor beds indicates that the formation of Ni-Fe alloy in the single-zone reactor bed promotes particle sintering and the high thermal stability of the eccentric core-shell structure prevents Ni and Fe particles in the bifunctional catalyst from sintering.

Based on the above conclusions, the double-zone bed with Fe/Zr@Zr-Ni@Zr bifunctional catalyst and Fe/Zr@Zr OSM offers optimal spatial structuring: it combines the highest activity and stability for catalyzing auto-thermal dry reforming of CH_4 with the better performance of the double-zone bed configuration for CO_2 utilization, providing a promising reactor technology for catalyst-assisted chemical looping auto-thermal dry reforming.

Acknowledgments

This work was supported by the “Long Term Structural Methusalem Funding by the Flemish Government”, the China Scholarship Council (CSC) and the Interuniversity Attraction Poles Programme IAP7/5, – Belgian State – Belgian Science Policy. The authors acknowledge support from Geert Rampelberg with the in-situ XRD equipment (Department of Solid State Sciences, Ghent University).

Appendix A. Supplementary data

Supplementary material related to this article can be found, in the online version, at doi:<https://doi.org/10.1016/j.apcatb.2018.03.004>.

References

- R.K. Singha, A. Shukla, A. Yadav, S. Adak, Z. Iqbal, N. Siddiqui, R. Bal, *Appl. Energy* 178 (2016) 110–125.
- V.V. Galvita, H. Poelman, C. Detavernier, G.B. Marin, *Appl. Catal. B Environ.* 164 (2015) 184–191.
- J. Ni, L. Chen, J. Lin, S. Kawi, *Nano Energy* 1 (2012) 674–686.
- I.H. Son, S. Kwon, J.H. Park, S.J. Lee, *Nano Energy* 19 (2016) 58–67.
- D. Pakhare, J. Spivey, *Chem. Soc. Rev.* 43 (2014) 7813–7837.
- V.M. Gonzalez-Delacruz, R. Pereñiguez, F. Ternero, J.P. Holgado, A. Caballero, *ACS Catal.* 1 (2011) 82–88.
- W. Chu, L.N. Wang, P.A. Chernavskii, A.Y. Khodakov, *Angew. Chem. Int. Ed. Engl.* 47 (2008) 5052–5055.
- X. Chen, J. Jiang, K. Li, S. Tian, F. Yan, *Appl. Energy* 185 (2017) 687–697.
- S. Corthals, J. Van Nederkassel, H. De Winne, J. Geboers, P. Jacobs, B. Sels, *Appl. Catal. B Environ.* 105 (2011) 263–275.
- A. Serrano-Lotina, L. Daza, *Int. J. Hydrogen Energy* 39 (2014) 4089–4094.
- Y.H. Taufiq-Yap, Sudarno, U. Rashid, Z. Zainal, *Appl. Catal. A Gen.* 468 (2013) 359–369.
- J.L. Ewbank, L. Kovarik, C.C. Kenvin, C. Sievers, *Green Chem.* 16 (2014) 885–896.
- S.A. Theofanidis, V.V. Galvita, H. Poelman, G.B. Marin, *ACS Catal.* 5 (2015) 3028–3039.
- S. Bhavsar, M. Najera, G. Veser, *Chem. Eng. Technol.* 35 (2012) 1281–1290.
- M.P. Kohn, M.J. Castaldi, R.J. Farrauto, *Appl. Catal. B Environ.* 94 (2010) 125–133.
- H. Zhao, L. Guo, X. Zou, *Appl. Energy* 157 (2015) 408–415.
- B. Christian Enger, R. Lødeng, A. Holmen, *Appl. Catal. A Gen.* 346 (2008) 1–27.
- W.-H. Chen, S.-C. Lin, *Appl. Energy* 162 (2016) 1141–1152.
- W.-H. Chen, M.-R. Lin, J.-J. Lu, Y. Chao, T.-S. Leu, *Int. J. Hydrogen Energy* 35 (2010) 11787–11797.
- V.R. Choudhary, K.C. Mondal, *Appl. Energy* 83 (2006) 1024–1032.
- M. Tang, L. Xu, M. Fan, *Appl. Energy* 151 (2015) 143–156.
- L. Neal, A. Shafiefarhood, F. Li, *Appl. Energy* 157 (2015) 391–398.
- A. Löfberg, T. Kane, J. Guerrero-Caballero, L. Jalowiecki-Duhamel, *Chem. Eng. Process. Process Intensif.* 122 (2017) 523–529.
- J. Hu, V.V. Galvita, H. Poelman, C. Detavernier, G.B. Marin, *J. CO₂ Util.* 17 (2017) 20–31.
- V.V. Galvita, H. Poelman, V. Bliznuk, C. Detavernier, G.B. Marin, *Ind. Eng. Chem. Res.* 52 (2013) 8416–8426.
- N.V.R.A. Dharanipragada, L.C. Buelens, H. Poelman, E. De Grave, V.V. Galvita, G.B. Marin, J. Mater. Chem. A 3 (2015) 16251–16262.
- M. Meledina, S. Turner, V.V. Galvita, H. Poelman, G.B. Marin, G. Van Tendeloo, *Nanoscale* 7 (2015) 3196–3204.
- L.F. de Diego, M. Ortiz, J. Adánez, F. García-Labiano, A. Abad, P. Gayán, *Chem. Eng. J.* 144 (2008) 289–298.
- G. Pantaleo, V. La Parola, F. Deganello, P. Calatozzo, R. Bal, A.M. Venezia, *Appl. Catal. B Environ.* 164 (2015) 135–143.
- L.F. de Diego, M. Ortiz, F. García-Labiano, J. Adánez, A. Abad, P. Gayán, *J. Power Sources* 192 (2009) 27–34.
- H.R. Forutan, E. Karimi, A. Hafizi, M.R. Rahimpour, P. Keshavarz, *J. Ind. Eng. Chem.* 21 (2015) 900–911.
- M. Johansson, T. Mattisson, A. Lyngfelt, *Chem. Eng. Res. Des.* 84 (2006) 807–818.
- M. Rydén, D. Jing, M. Källén, H. Leion, A. Lyngfelt, T. Mattisson, *Ind. Eng. Chem. Res.* 53 (2014) 6255–6267.
- I. Adánez-Rubio, P. Gayán, A. Abad, F. García-Labiano, L.F. de Diego, J. Adánez, *Chem. Eng. J.* 256 (2014) 69–84.
- J. Hu, L. Buelens, S.-A. Theofanidis, V.V. Galvita, H. Poelman, G.B. Marin, *J. CO₂ Util.* 16 (2016) 8–16.
- L.C. Buelens, V.V. Galvita, H. Poelman, C. Detavernier, G.B. Marin, *Science* 354 (2016) 449–452.
- V.V. Galvita, H. Poelman, G.B. Marin, *Top. Catal.* 54 (2011) 907–913.
- N.L. Galinsky, A. Shafiefarhood, Y. Chen, L. Neal, F. Li, *Appl. Catal. B Environ.* 164 (2015) 371–379.
- H.P. Hamers, F. Gallucci, P.D. Cobden, E. Kimball, M. van Sint Annaland, *Int. J. Greenh. Gas Control* 16 (2013) 1–12.
- Z. Zhou, *Aerosol Air Qual. Res.* 14 (2014) 559–571.
- L. Du, L. Luo, Z. Feng, M. Engelhard, X. Xie, B. Han, J. Sun, J. Zhang, G. Yin, C. Wang, Y. Wang, Y. Shao, *Nano Energy* 39 (2017) 245–252.
- H. Tian, X. Li, L. Zeng, J. Gong, *ACS Catal.* 5 (2015) 4959–4977.
- E. Bakta, P. Littlewood, R. Schomäcker, A. Thomas, P.C. Stair, *Appl. Catal. B Environ.* 179 (2015) 122–127.
- Z. Xu, H. Zhao, Y. Wei, C. Zheng, *Combust. Flame* 162 (2015) 3030–3045.
- V. Srdic, B. Mojic, M. Nikolic, S. Ognjanovic, *Process. Appl. Ceram.* 7 (2013) 45–62.
- J.B. Yoo, H.S. Kim, S.H. Kang, B. Lee, N.H. Hur, J. Mater. Chem. A 2 (2014) 18929–18937.
- Y. Yang, J. Liu, X. Li, X. Liu, Q. Yang, *Chem. Mater.* 23 (2011) 3676–3684.
- W. Stöber, A. Fink, J. Colloid Interface Sci. 26 (1968) 62–69.
- P.M. Arnal, C. Weidenthaler, F. Schüth, *Chem. Mater.* 18 (2006) 2733–2739.
- I. Chorkendorff, J.W. Niemantsverdriet, *Concepts of Modern Catalysis and Kinetics*, Wiley, Hoboken, NJ, USA, 2006.
- J. Ashok, S. Kawi, *ACS Catal.* 4 (2014) 289–301.
- T.D. Shen, I. Shmagin, C.C. Koch, R.M. Kolbas, Y. Fahmy, L. Bergman, R.J. Nemanich, M.T. McClure, Z. Sitar, M.X. Quan, *Phys. Rev. B Condens. Matter* 55 (1997) 7615–7623.
- W. Cai, L. Ye, L. Zhang, Y. Ren, B. Yue, X. Chen, H. He, *Materials* 7 (2014) 2340–2355.
- T. Yamaguchi, *Catal. Today* 20 (1994) 199–218.
- S. Li, C. Zhang, Z. Huang, G. Wu, J. Gong, *Chem. Commun. (Camb.)* 49 (2013) 4226–4228.
- D. King, J. Strohm, X. Wang, H. Roh, C. Wang, Y. Chin, Y. Wang, Y. Lin, R. Rozmiarek, P. Singh, *J. Catal.* 258 (2008) 356–365.
- Y. Han, W. Yan, *Water Res.* 66 (2014) 149–159.
- K. Fukudome, A. Kanno, N.-o. Ikenaga, T. Miyake, T. Suzuki, *Catal. Lett.* 141 (2010) 68–77.
- H.C. Zeng, J. Lin, W.K. Teo, F.C. Loh, K.L. Tan, *J. Non-Cryst. Solids* 181 (1995) 49–57.
- Y. He, Y. Wu, T. Chen, W. Weng, H. Wan, *Catal. Commun.* 7 (2006) 268–271.
- R. Wojcieszak, *Appl. Catal. A Gen.* 268 (2004) 241–253.
- A. Djaidja, A. Barama, M.M. Bettahar, *Catal. Today* 61 (2000) 303–307.
- W. Yoon, J. Hanson, J. McBreen, X. Yang, *Electrochim. Commun.* 8 (2006) 859–862.
- W.A.W.A. Bakar, M.Y. Othman, R.A.C.K. Yong, S. Toemen, *Mod. Appl. Sci.* 35–43 (2009).
- M. Dickinson, T.B. Scott, R.A. Crane, O. Riba, R.J. Barnes, G.M. Hughes, *J. Nanopart. Res.* 12 (2009) 2081–2092.
- N. Moghimi, S. Bazargan, D. Pradhan, K.T. Leung, *J. Phys. Chem. C* 117 (2013) 4852–4858.
- J. Ashok, S. Kawi, *Appl. Catal. A Gen.* 490 (2015) 24–35.
- J. Gao, Z. Hou, X. Liu, Y. Zeng, M. Luo, X. Zheng, *Int. J. Hydrogen Energy* 34 (2009) 3734–3742.
- A. Cadi-Essadek, A. Roldan, N.H. de Leeuw, *Surf. Sci.* 653 (2016) 153–162.
- X. Zhang, Q. Zhang, N. Tsubaki, Y. Tan, Y. Han, *Fuel* 147 (2015) 243–252.
- M. Yamasaki, H. Habazaki, K. Asami, K. Izumiya, K. Hashimoto, *Catal. Commun.* 7 (2006) 24–28.
- S.A. Theofanidis, R. Batchu, V.V. Galvita, H. Poelman, G.B. Marin, *Appl. Catal. B Environ.* 185 (2016) 42–55.